ChemComm

HIGHLIGHT

View Article Online
View Journal | View Issue

Cite this: *Chem. Commun.*, 2024, **60**, 9310

Chiral 2D and quasi-2D hybrid organic inorganic perovskites: from fundamentals to applications

Marco Moroni, * Clarissa Coccia and Lorenzo Malavasi *

Received 3rd July 2024,
Accepted 31st July 2024

DOI: 10.1039/d4cc03314k

rsc.li/chemcomm

Chiral 2D and quasi-2D hybrid organic–inorganic perovskites (HOIPs) are emerging as promising materials for a variety of applications principally related to optoelectronics and spintronics, thanks to the combined benefits deriving from both the chiral cation and the perovskite structure. Since its recent birth, this research field is tremendously growing, focalizing on the chemical composition tuning to unveil its influence on the related functional properties as well as on developing devices for practical applications. In this review, we focused on the properties of 2D and quasi-2D chiral HOIPs, firstly providing an overview on their chiroptical behaviour followed by their potential exploitation in devices investigated so far for various applicative fields.

Introduction

General overview

In the last decades the research interest towards hybrid organic–inorganic perovskites (HOIPs) has widely increased due to their promising applications in many fields, such as photovoltaics, photodetection, optoelectronics, technologies based on light-emitting diodes (LEDs), energy harvesting and photocatalysis.[1–6] Indeed, these materials do possess outstanding light absorption in the UV, visible and even infrared spectral regions, as well as tunable emission with remarkable quantum yields.[7] In addition to these advantages, it is possible to employ chiral molecules as organic cations imparting chirality to the perovskite itself, by virtue of a mechanism known as chirality transfer, whose fundamentals are currently being examined.[8] Therefore, chiral HOIPs combine the above-described optical properties with the capability of discriminating the polarized light, thus displaying superior circular dichroism (CD) or circularly polarized luminescence (CPL) as well as an intrinsic spin selectivity.

Despite the above listed promising characteristics, the field of chiral perovskites is still at an early stage. Indeed, the first example appeared in 2003, when Billing and Lemmerer reported the crystal structure of the 1D system (*S*-MBA)$PbBr_3$ (MBA = α-methylbenzylamine),[9] followed in 2006 by the 2D

Department of Chemistry and INSTM, University of Pavia, Via Taramelli 12, 27100 Pavia, Italy. E-mail: lorenzo.malavasi@unipv.it

Marco Moroni

Marco Moroni earned his PhD in Chemical Sciences from the University of Insubria in 2023. Then, he started his role as a post-doctoral fellow at the University of Pavia. In 2024, he began working as the Principal Investigator of the project "Engineering chiral perovskites: developing novel and efficient materials for future and sustainable electronics (CHIRO4FUTURE)" funded by Fondazione Cariplo. His research is focused on the synthesis, structural characterization, and functional analysis of chiral perovskites, with emphasis on the relationships between crystal structure and chiroptical properties.

Clarissa Coccia

Clarissa Coccia is a native of Pavia (Italy). She completed her bachelor's and master's degree in Chemistry at the University of Pavia cum laude. She is currently a PhD student at University of Pavia in Lorenzo Malavasi's group "Energy and Materials Chemistry Group". Her research is focused on the synthesis and the structural characterization of lead-free chiral perovskites, with a particular focus on single crystal growth and the exploitation of possible correlations between structure and chiroptical properties.

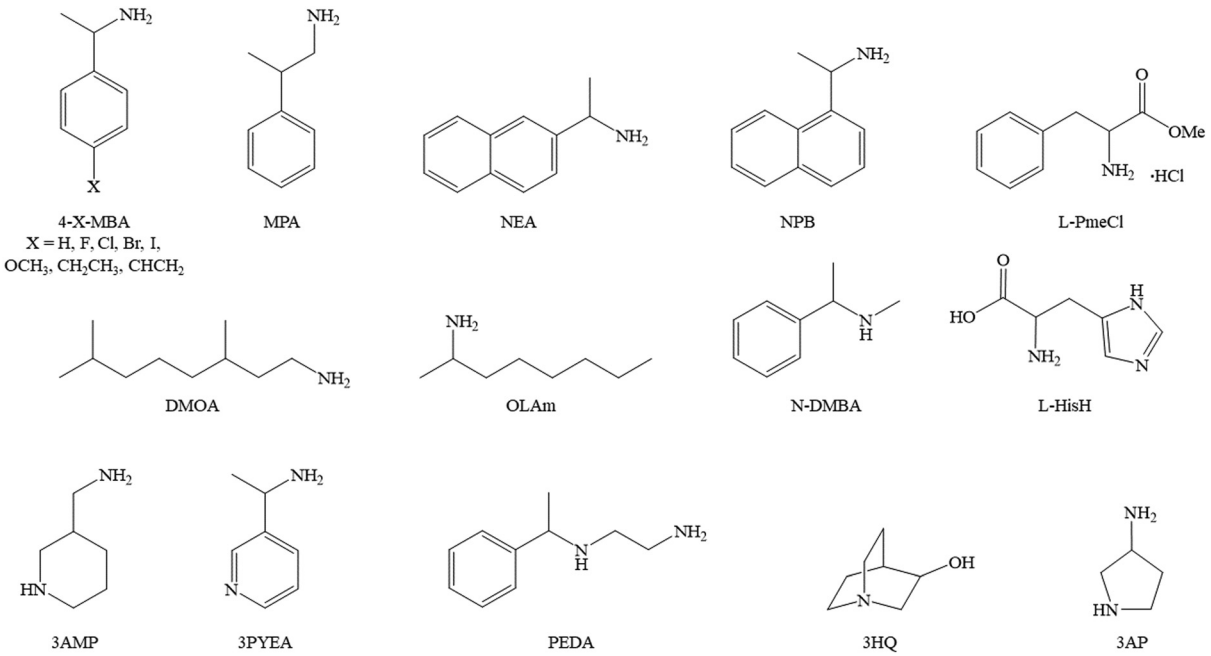

Fig. 1 Structural formulas of the main organic cations employed so far in the synthesis of chiral perovskites.

$(R/S\text{-MBA})_2PbI_4$.[10] However, their chiroptical properties started being deeply investigated only in 2017 with the groundbreaking work of Ahn and co-workers,[11] pioneering a field which is in continuous growth. Indeed, up to date, chiral HOIPs have been studied for different purposes spanning from the optical properties, the spin-related features such as the Rashba–Dresselhaus (RD) spin-splitting or the chirality induced spin selectivity (CISS), and the ferroelectric and piezoelectric properties.[12–15] So far, the research on chiral HOIPs has mainly centred on 2D and quasi-2D materials, employing a number of different commercial chiral cations (Fig. 1) and also tuning the halogen and, more rarely, the metal center, to evaluate their impact on the functional properties. On the contrary, investigation on 1D and 0D perovskite derivatives are scarce,[16] and, in addition, lead has been the most investigated metal center despite its well-known toxicity, the latter highlighting the need for prompting the research field toward less toxic and more sustainable metal cations.

In this landscape, this review focuses on 2D and quasi-2D perovskites, presented here based on the employed chiral organic cation. Among the investigated properties, we mostly focused on the chiroptical behavior highlighting the influence of the various components, *i.e.* the chiral cations, the metal center and the halogen atoms, on such response. We further classified the 2D perovskites in lead-based and lead-free systems to highlight role of metal ion. Final section provides an overview of the devices reported in the literature so far, to highlight their potential in emerging technologies such as photodetection, photocatalysis, spin-LEDs and so on.

Lorenzo Malavasi

Lorenzo Malavasi is Full Professor of Physical Chemistry at the Chemistry Department of the University of Pavia. His current research interests are in the area of solid-state chemistry and devoted to the design of novel and optimized materials for clean energy applications such as hybrid organic–inorganic perovskites and catalysis materials. He is Director of the INSTM National Reference Centre "PREMIO" devoted to the synthesis of innovative materials and Editor of Journal of Physics and Chemistry of Solids.

Chirality and related optical properties

By definition, chirality is the property of an object of not being superimposable to its specular counterpart. Practically, this means that chiral materials must not contain S_n symmetry elements, such as mirror planes or inversion centers, condition achieved only if they crystallize in one of the 65 Shohncke space groups.[17] From a functional perspective, chiral materials feature an intriguing behaviour upon irradiation with polarized light, preferentially interacting with the left- or right-handed component (LCP or RCP, respectively). This property can be investigated by a number of characterization methods, of which the most widely employed are the CD and CPL, related to the chirality in the ground and excited states, respectively. Indeed, CD refers to the preferential absorption of LCP or RCP, while CPL is related to its preferential emission. The intensity of a CD

signal is the ellipticity (θ), measured in mdeg, which is numerically related to the difference in absorbance between LCP and RCP. Its magnitude can be quantified by the absorption dissymmetry factor (g_{CD}), which is calculated as:

$$g_{CD} = \frac{\theta}{32\,982 \cdot A}$$

where A represents the absorbance.

Similarly, the difference in LCP and RCP emission can be quantified with the emission dissymmetry factor (g_{CPL}) which is calculated as:

$$g_{CPL} = \frac{2(I_L - I_R)}{I_L + I_R}$$

where I_L and I_R are the LCP and RCP intensities, respectively.

Generation of 2D and quasi-2D chiral HOIPs

The term perovskite was firstly attributed to $CaTiO_3$, an inorganic mineral discovered on the Ural mountains, and derives from the Russian collector of minerals Perovskij. Taking inspiration from its crystal structure, several modulations of the chemical composition have been performed, allowing for the generation of a plethora of intriguing materials. Hence, the term perovskite is nowadays referred to a 3D material featuring ABX_3 chemical formula, where A is a monovalent cation, B is a divalent one and X is an halogen atom. Importantly, its structural formula is composed of corner sharing BX_6^{4-} octahedra forming cavities which are occupied by the A cations (Fig. 2a). However, the radius of A cation is regulated by the Goldschmidt tolerance factor, who guarantees a proper dimension for the cation to be accommodated in the hollows, condition which is difficult to be obtained when dealing with chiral organic molecules. Hence, to date, chiral 3D HOIPs remain in the theoretical development stage, since their instability rules out their synthesis. On the contrary, 2D and quasi-2D chiral HOIPs have been widely reported, which can be regarded as an horizontal slicing of the 3D framework allowing for the organic cations to be accommodated in form of layers sandwiching the inorganic corner-sharing sheets (Fig. 2b).[18] Pure 2D perovskites generally display the A_2BX_4 stoichiometry, while quasi-2D ones feature a $A_2A'_{n-1}B_nX_{3n+1}$ general formula, where A′ is a less steric hindered cation obeying the Goldschmidt tolerance factor and n is the number of inorganic layers separated by the bulky organic molecules. Ideally, n can vary from 1, corresponding to the A_2BX_4 2D HOIP, to infinite, yielding the archetypal 3D perovskite framework. The interest in quasi-2D perovskites derives from their intermediate characteristics between 3D and 2D phases, allowing to gain benefits from both of them. In particular, during photoexcitation, the photocarriers quickly move from higher to lower bandgap species, generating accumulation of carriers close to the recombination centers. This carrier density then effectively passivates the defect states, leading to an enhancement of the radiative recombination efficiency thus increasing the photoluminescence quantum yield (PLQY).[19]

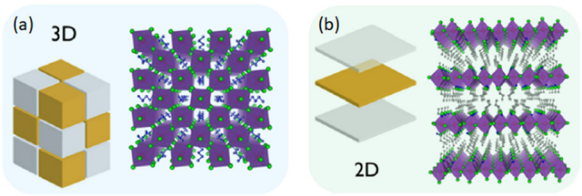

Fig. 2 Pictorial representation of (a) 3D and (b) 2D perovskite crystal structures. Reprinted with permission from ref. 18 Copyright©2017 American Chemical Society.

Lead-based 2D HOIPs

HOIPs with α-methylbenzylammonium (MBA)

$(MBA)_2PbI_4$ can be regarded as the most iconic chiral HOIP, as well as the forefather of this class of materials. Its two enantiomers, firstly synthesized by Billing and co-workers in 2006 and structurally characterized by single-crystal X-ray diffraction (SC-XRD), are enantiomorphic each other and crystallize in the $P2_12_12_1$ Shoncke space group. Each PbI_6^{4-} octahedron is corner-shared with four adjacent ones through its equatorial iodide atoms, forming infinite sheets in the ab plane (Fig. 3). The organic cations occupy the gap between neighboring inorganic sheets, forming hydrogen bonds through the amino groups with the axial iodide atoms.[10]

On the other hand, the racemic compound crystallizes in the centrosymmetric $P2_1/a$ space group, hence featuring inversion and mirror plane symmetry elements, and displays a similar 2D layered structure.[20]

The first chiroptical investigation on $(R/S/Rac\text{-MBA})_2PbI_4$ appeared in 2017 by Ahn and co-workers, who measured the CD on HOIPs thin films attaining signals with opposite sign at the same wavelength (367, 408, 489 and 501 nm) for the two enantiomers and a rather flat curve for the racemic (Fig. 4). These λ are significantly different from those of the pure R/S-MBA, which are found around 260 nm, confirming that the chirality is transferred to the HOIPs. Moreover, the signals of $(R/S/Rac\text{-MBA})_2PbI_4$ change sign in correspondence to the exciton absorption edge, which could be ascribed to the Cotton effect. The authors reported a g_{CD} of 6×10^{-3}, a value that was

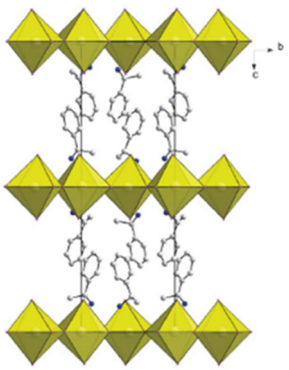

Fig. 3 Packing diagram of $(R\text{-MBA})_2PbI_4$. Reprinted with permission from ref. 10 Copyright©2006 Royal Society of Chemistry.

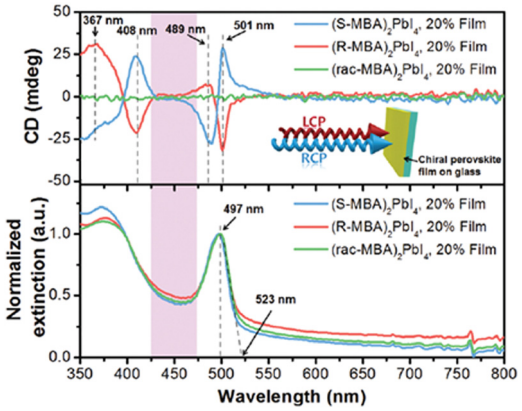

Fig. 4 Transmission CD spectra (above) and normalized extinction spectra (below) of (*R*/*S*/*Rac*-MBA)$_2$PbI$_4$ (in the inset a pictorial representation of a HOIP thin film irradiated by LCP/RCP light). Reprinted with permission from ref. 11 Copyright©2017 Royal Society of Chemistry.

one order of magnitude greater than the chiral quantum dots published until then.[11]

In 2019 Ma and colleagues focused on the photoluminescence (PL) emission of (*R*/*S*/*Rac*-MBA)$_2$PbI$_4$, observing PL peaks at around 510 nm, in line with the absorption spectra and characteristic of free exciton (FE) emission. Moreover, they reported a long tail at higher wavelengths that might be ascribed to self-trapped exciton (STE) emission, as commonly observed in 2D HOIPs. They studied the CPL response as well (Fig. 5) highlighting an average g_{CPL}, *i.e.* mediated on the measured microplates, of 9.6% and 10.1% at 77 K for the *R* and *S* enantiomers, respectively, and a maximum g_{CPL} of 17.6% in (*S*-MBA)$_2$PbI$_4$. This discrepancy between the mean and the maximum values can be associated with the different thickness of the measured microplates, which is known to influence the amount of absorbed light. By measuring the CPL as a function of temperature, the authors discovered that g_{CPL} monotonously decreases while increasing the temperature, suggesting a decrease of the chirality transfer. They formulated diverse hypotheses to rationalize this occurrence, among which a decreasing of the octahedra distortion caused by the increase of the electron–phonon interactions and thermal expansion.[21]

Noteworthy, for practical applications, (*R*/*S*/*Rac*-MBA)$_2$PbI$_4$ is stable for at least 7 days in form of thin films (stored at 298 K and 20% humidity)[11] and 2 months as powder under ambient conditions.[21]

In the same year, Wang *et al.* developed a new synthetic protocol for synthesizing (*R*/*S*/*Rac*-MBA)$_2$PbI$_4$, working in water at room temperature and controlling the pH. Measuring the CPL the authors reported g_{CPL} values of 13.7% and 11.4% at room temperature and correlated this enhancement to the better quality of the crystals synthesized with this new method.[22]

In 2020 Ahn and collaborators investigated the chemical composition effect on the CD signal by synthesizing the solid solutions (*R*/*S*-MBA)$_2$PbI$_{4(1-x)}$Br$_{4x}$ with x values of 0, 0.1, 0.2, 0.3, 0.4, and 0.5. Starting from $x = 0$ (iodide), they reported a CD blue-shift up to $x = 0.3$, where the maximum passes from 495 to 474 nm (Fig. 6). After this composition, a structural transition occurs prompted by the non-random distribution of iodide and bromide anions in the solid solution that caused a structural rearrangement, and consequently the CD signal is switched off. To further blue shift the CD signal the authors moved to a bigger chiral cation, namely *R*/*S*-NEA, synthesizing the solid solutions and observing active CD signal in the bromide determinant phase (see below).[23]

Zhou *et al.* synthesized the pure (*R*-MBA)$_2$PbBr$_4$ as well as (*R*-4-X-MBA)$_2$PbBr$_4$ (X = F, Cl, Br) to study the effect of the *para* substituent on the optical properties. Based on a literature example carried out on different (and achiral) HOIPs,[24] thus without solving the crystal structure, they proposed a structural change from Ruddlesden–Popper (RP) to near Dion–Jacobson (DJ) passing from *R*-MBA to *R*-4-X-MBA due to halogen-involving interactions inducing disorder in the Pb–Br–Pb angle. These occurrence causes the energy gap to reduce in the halogen substituted HOIPs leading to a red-shift in the absorption spectrum and a broad emission in the PL, typical of STE

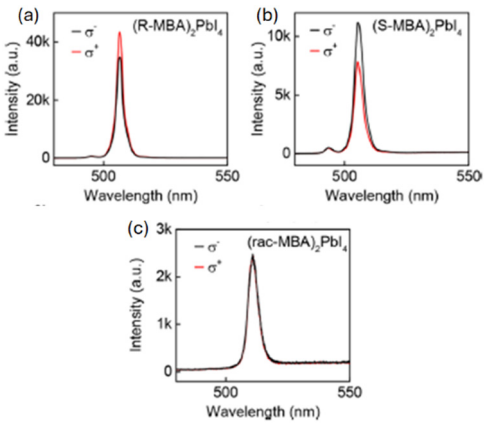

Fig. 5 CPL spectra of (a) (*R*-MBA)$_2$PbI$_4$, (b) (*S*-MBA)$_2$PbI$_4$ and (c) (*Rac*-MBA)$_2$PbI$_4$ excited by a 473 nm laser at 77 K. Left-handed light, σ^-; right-handed light, σ^+. Reprinted with permission from ref. 21 Copyright©2019 American Chemical Society.

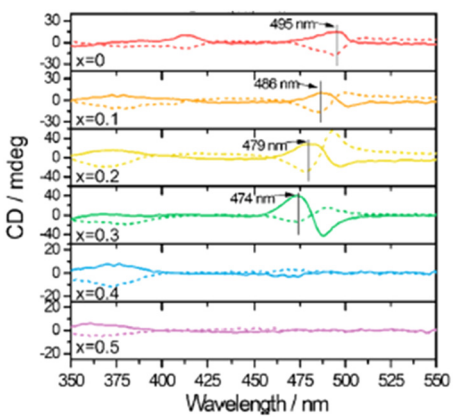

Fig. 6 CD spectra of (*R*/*S*-MBA)$_2$PbI$_{4(1-x)}$Br$_{4x}$. Solid line, *S* enantiomer; dashed line, *R* enantiomer. Reprinted with permission from ref. 23 Copyright©2020 American Chemical Society.

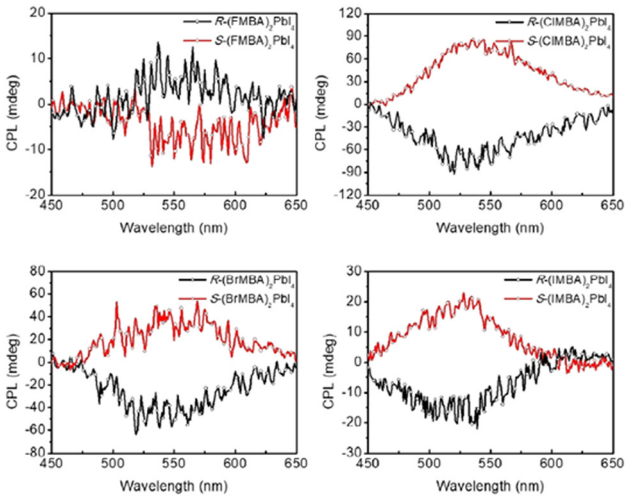

Fig. 7 CPL spectra of (R/S-4-X-MBA)$_2$PbI$_4$, X = F, Cl, Br, I. Reprinted with permission from ref. 26 Copyright©2021 Wiley-VCH GmbH.

emission and different from the sharper peak displayed by (R-MBA)$_2$PbBr$_4$ and ascribed to FE emission. Moreover, time-resolved PL indicated longer decay time for the halogen substituted compounds and a higher PLQY, reaching 16.97% in Cl-substituted compound (*vs.* 3.43% of (R-MBA)$_2$PbBr$_4$). Interestingly, the authors found out a CD signal up to 15 mdeg for (R-MBA)$_2$PbBr$_4$ and an increase in (R-4-X-MBA)$_2$PbBr$_4$, indicating that the halogen can enhance the chirality intensity.[25]

In 2021 Lin and co-workers carried out a similar study on (R/S/*Rac*-MBA)$_2$PbI$_4$ as well as (R/S/*Rac*-4-X-MBA)$_2$PbI$_4$ (X = F, Cl, Br, I). By evaluating the PXRD patterns carried out on thin films they reported a d-spacing increase with the substituent trend H < F < Cl < Br < I, as expected based on their atomic radius. Interestingly, by measuring the CD, they observed g_{CD} values of 20 mdeg for (R/S-MBA)$_2$PbI$_4$, a drop to 10 mdeg for (R/S-4-F-MBA)$_2$PbI$_4$, and an enhancement to 90 mdeg in (R/S-4-Cl-MBA)$_2$-PbI$_4$, followed by a decrease to 60 and 30 mdeg in (R/S-4-Br-MBA)$_2$PbI$_4$ and (R/S-4-I-MBA)$_2$PbI$_4$, respectively. Moreover, the CPL (Fig. 7) features the highest value for the Cl-substituted HOIP while the lowest for the F-substituted one, in line with the trend disclosed by CD. The authors associated the g_{CD} trend to an interplay of d-spacing and structural features. Indeed, while the d-spacing enhancement causes a lowering of the rotational strength, a diverse disposition of the organic cation observed through SC-XRD analysis passing from (R/S-4-F-MBA)$_2$PbI$_4$ to (R/S-4-Cl-MBA)$_2$PbI$_4$, unveiled that Cl interacts with the iodide anions more than F, leading to a more regular structure (near DJ phase) and a stronger angular momentum for the entire HOIPs.[26]

In the same year, Pan *et al.* investigated the influence of both the temperature and the magnetic field on the CPL emission of (R/S-MBA)$_2$PbI$_4$. Measuring the CPL from 4 to 300 K the authors retrieved a P_c value (which is defined as g_{CPL} divided by 2) opposite in sign and similar in modulus for the two enantiomers, which decreases as the temperature raises (Fig. 8). Moreover, by applying an external magnetic field of ±900 mT, the authors unveiled, as a function of the magnetic field sign, a decrease in the P_c of one enantiomer concomitant with the

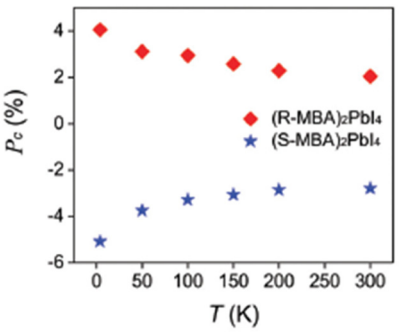

Fig. 8 Temperature-dependent CPL for (R/S-MBA)$_2$PbI$_4$. Reprinted with permission from ref. 27 Copyright©2022 Royal Society of Chemistry.

enhancement of the other, in addition to the P_c value reduction caused by the temperature effect.

The role of the magnetic field was confirmed by an experiment carried out at 4 K varying the magnetic field from −900 to +900 mT, where the P_c steadily increases with positive values for (R-MBA)$_2$PbI$_4$ while decreases with negative values for (S-MBA)$_2$PbI$_4$. The authors related this behaviour to the spin–orbit coupling (SOC) displayed by chiral HOIPs, hence to the interaction between the exciton fine structure and the magnetic field. Finally, they claimed that this investigation indicates that the magnetic field is an effective tool to manipulate both the polarization and the intensity of the CPL in chiral perovskites, thus providing a promising approach for novel device applications.[27]

In 2022 Ma and colleagues investigated the solid solution (R/S/*Rac*-MBA$_2$)PbI$_{4(1-x)}$Br$_{4x}$, nanoconfining the material growth by using anodized aluminum oxide (AAO) with different porosities, namely 66, 100 and 112 nm. Starting from the composition with x = 0.325, they reported a significant enhancement of the g_{CD} moving from the planar material (3.8×10^{-4}) to the ones grown in AAO, with a maximum value of -2×10^{-3} when the AAO porosity is 100 nm. Noteworthy the CD signal is flat in all samples for the racemic compounds, indicating that AAO does not influence the g_{CD}. The same increment in g_{CD} for the nanoconfined HOIPs *vs.* the planar ones was also observed in samples with different x, *i.e.* with a different I *vs.* Br ratio. For x = 0.325 the authors measured the CPL, attaining a clear FE emission for the 100 nm AAO templated HOIP with g_{CPL} of 6.4×10^{-2} and -4.4×10^{-2} for the R and S enantiomers, respectively. This effect was rationalized on the basis of the microstrain generated by the nanoconfined growth, which induces a reorientation of the organic ligands and thus an enhancement of the π–π stacking interactions, as supported by DFT calculations. This occurrence can increase the electronic interactions between the organic and inorganic parts leading to an amplification of the chirality transfer.[28]

In 2023 Lu *et al.* evaluated the effect of mixing chiral and achiral organic cations obtaining the material with nominal composition (R/S-MBA$_x$PEA$_{(1-x)}$)$_2$PbBr$_4$ with x = 0.75 (PEA = phenylethylammonium), which featured a strong CD signal at the excitonic absorption maxima, in sharp contrast with the pure chiral (R/S-MBA)$_2$PbBr$_4$ (Fig. 9). As evidenced by ^{1}H-NMR and DFT calculations, the PEA binding energy is higher than the MBA one, leading to an enhanced material stability which is

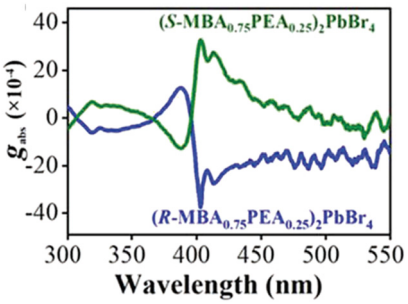

Fig. 9 g_{CD} values of (*R*/*S*-$MBA_{0.75}PEA_{0.25})_2PbBr_4$. Reprinted with permission from ref. 29 Copyright©2022 Wiley-VCH GmbH.

confirmed by the thermogravimetric analysis (TGA) decomposition onset. The authors also stated that the less steric hindrance around the amino group is another factor beneficial for the stability enhancement. Moreover, the different binding energy promoted the defect passivation of the nanosheets suppressing the non-radiative recombination of the charge carriers, thus leading to an enhancement of the chiroptical behaviour. Indeed, time-resolved PL on samples with nominal *x* of 0.25, 0.5 and 0.75 indicated significantly longer decay times in the alloyed samples than in the pure chiral one.[29]

Zhao and collaborators substituted MBA with vinyl and ethyl groups in the *para* position, promoting in the former an *in situ* cross-linking polymerization compared to the latter which did not polymerize. The authors observed that the polymerization increased the stability both under environmental conditions and UV exposure. Comparing the CD response, no significant variations were reported in the two cases, although the polymerized sample featured a slightly higher signal with values over 40 mdeg. However, by monitoring the CD signal as a function of UV exposure time, the authors observed a signal stable for 60 minutes in the polymerized HOIP while a substantial decrease in the not-polymerized one (Fig. 10).[30]

In 2024 Scalon *et al.* investigated the solvent role in the formation of (*R*/*S*/*Rac*-MBA)$_2PbI_4$ thin films by utilizing two solvents featuring different coordination ability with lead, namely dimethylformamide (DMF) and acetonitrile (ACN). Indeed, ACN is known to be less coordinant with respect to DMF and to induce a faster crystallization. The authors demonstrated that thin films of $(MBA)_2PbI_4$ feature impurities of the 1D phase $(MBA)PbI_3$, the extent of which depends on whether the HOIP is chiral or racemic and on the nature of the solvent. In particular, the 1D phase content is higher with ACN than DMF and decreases passing from the chiral samples to the racemic, being absent in the DMF-prepared (*Rac*-MBA)$_2PbI_4$. Moreover, the films prepared with DMF display a bigger crystal size. These occurrences affect conductivity and chiroptical properties: the in-plane conductivity is indeed significantly higher in the DMF-prepared thin films while the g_{CD} is enhanced by the 1D impurities of the ACN-prepared ones, demonstrating that tuning the phase purity in 2D HOIPs is an important tool for practical applications.[31]

The same group then adopted another strategy to modulate the content of 1D $(MBA)PbI_3$ impurities, namely inserting a methoxy group in the *para* position of the MBA cations, thus synthesizing (*R*/*S*/*Rac*-*p*OMeMBA)$_2PbI_4$ where *p*OMeMBA is *para*-methoxy-α-methylbenzylammonium. The first observation comes from the *d*-spacing which is less than twice the sum of the cation length (as we are dealing with RP HOIPs) in the case of *p*OMeMBA)$_2PbI_4$, indicating, for this compound, a more favourable crystal packing. Moreover, XRD did not detect 1D impurities in the methoxy-substituted HOIP. The authors reported that the CD signal of (*R*/*S*-*p*OMeMBA)$_2PbI_4$ is significantly reduced compared to that of (*R*/*S*-MBA)$_2PbI_4$ plausibly because of the increased interlayer distance which influences the chirality transfer. On the other hand, by comparing the PL emissions for the two compounds as a function of temperature (Fig. 11), they found out a more symmetric peak for the methoxy-substituted HOIP, while the unsubstituted featured a shoulder at lower energies with STE character, with an increasing contribution as the temperature raised. Overall, the authors indicated that the insertion of a *para*-methoxy group on the chiral MBA cations led to a narrower and more symmetric PL emission band concomitant with a higher PLQY at room temperature (0.14%).[32]

Aiming at increasing the octahedral tilting of (*R*/*S*-MBA)$_2PbI_4$, Kim and collaborators coupled the title HOIP with the helical mesoscopic structure formed by the (4,4′,4″,4‴-(porphine-5,10,15,20-tetrayl)tetrakis(benzenesulfonic acid)), as this molecule is known to helically stack when stabilized with chiral ligands (Fig. 12). The authors reported a reduction of the PLQY and an increase in the tensile strain of the attained assembly, occurrences evidencing close interactions among the

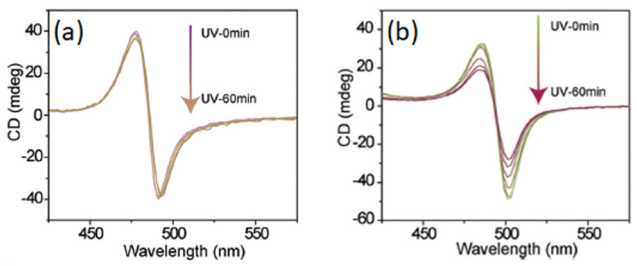

Fig. 10 CD spectra of (a) polymerized and (b) unpolymerized (*S*-R-MBA)$_2PbI_4$ Reprinted with permission from ref. 30 Copyright©2023 Wiley-VCH GmbH.

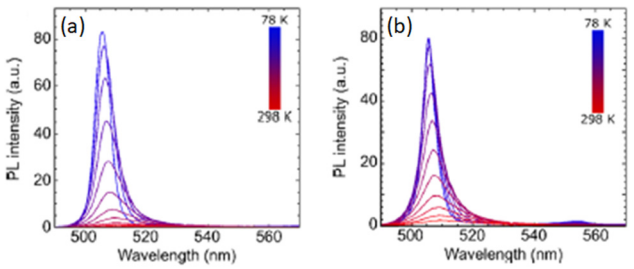

Fig. 11 PL spectra acquired as a function of the temperature for (a) (*R*-MBA)$_2PbI_4$ and (b) (*R*-pOMeMBA)$_2PbI_4$. Reprinted with permission from ref. 32 Copyright©2024 American Chemical Society.

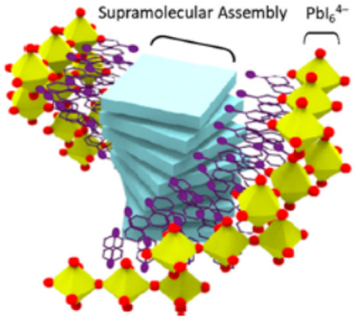

Fig. 12 Pictorical representation of the helical supramolecular assembly. Reprinted with permission from ref. 33 Copyright©2024 American Chemical Society.

perovskite and the molecular helices. Measuring the CD they found out a 2.7 fold increase in the g_{CD}, from 3.7×10^{-4} to 1×10^{-3}, passing from the pure $(S\text{-MBA})_2PbI_4$ to the helically coupled HOIP, and associated this result to the concomitant effect of (i) an increased lattice distortion in perovskites ingenerated by the perovskite-supramolecular coassembly, and (ii) the structural chirality due the helical perovskite and supramolecular coassembly structures.[33]

HOIPs with β-methylphenethylammonium (MPA)

The first crystal structure solution of the 2D chiral perovskite $(R/S/Rac\text{-MPA})_2PbBr_4$ appeared in 2020 by Trujillo-Hernández and co-workers, who reported a mirrored network for the two enantiomers, crystallizing in the non-centrosymmetric space group $P2_12_12_1$, and a non-chiral crystal structure displaying the centrosymmetric space group *Pbca* for the racemic compound (Fig. 13). All of them feature corner-sharing $PbBr_6^{4-}$ distorted octahedra separated by a bilayer of organic cations. Noteworthy, a material with the same A, B and X constituents was already structurally characterized by Yuan *et al.* in 2018, but reporting a metal halide with $(R/S\text{-MPEA})_{1.5}PbBr_{3.5}(DMSO)_{0.5}$ stoichiometry, displaying half of the octahedra reciprocally edge-sharing and coordinated dimethylsulfoxide (DMSO) coming from the solvent.[34] The authors

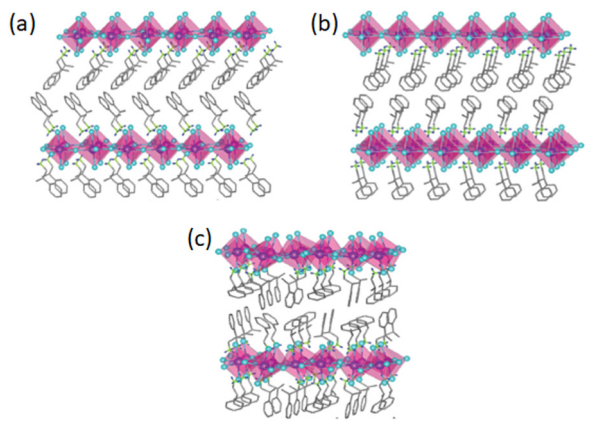

Fig. 13 Crystal structure of (a) $(R\text{-MPA})_2PbBr_4$, (b) $(S\text{-MPA})_2PbBr_4$ and (c) $(Rac\text{-MPA})_2PbBr_4$. Reprinted with permission from ref. 35 Copyright©2020 Royal Society of Chemistry.

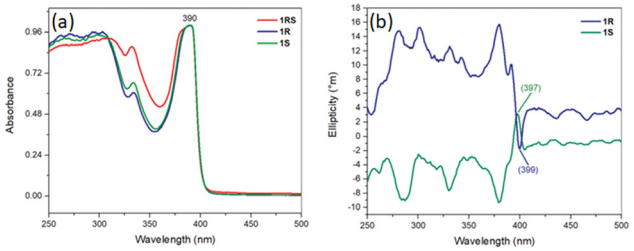

Fig. 14 (a) UV visible absorption and (b) CD spectra of $(R/S/Rac\text{-MPA})_2PbBr_4$. Reprinted with permission from ref. 35 Copyright©2020 Royal Society of Chemistry.

reported that $(R/S/Rac\text{-MPA})_2PbBr_4$ features UV-Vis absorption at *ca.* 390 nm (Fig. 14a), similar for all the materials, and a substantial CD response in both excitonic and bandgap spectral regions, with peaks at approximately the same positions but with oppositely signed values (Fig. 14b). The CD spectra of both enantiomers cross zero and change signs close to the exciton absorption, as expected as a consequence of the Cotton effect.[35]

In 2021, Ren *et al.* synthesized $(R/S\text{-MPA})_2PbBr_4$ in form of nanosheets (NSs) employing octylamine (OA) as protecting agent. The authors demonstrated for the first time intrinsic chirality in perovskite NSs and stated that this occurrence is allowed by the enhanced distance of the amino group from the phenyl ring which diminishes the cation steric hindrance close to the octahedra. Indeed, the authors also synthesized the analogue X_2PbBr_4 perovskites NSs with X = *R*-2-butylamine, *R*-2-hexylamine and *R*-MBA attaining very low UV-Vis absorptions and negligible CD signals. They then focused on optimizing the *R*/*S*-MPABr to $PbBr_2$ molar ratio and the OA amount to maximize the chiroptical properties. They found out that the higher CD signal, corresponding to a g_{CD} of 6×10^{-3}, was obtained when MPABr:$PbBr_2$ = 5 : 2 and 1 μL of OA (Fig. 15). Indeed, a strong CD response requires a balance between the chiral component and the protecting agent. Without protecting agent there is the highest fraction of chiral molecule, but the NSs are poorly stable, negatively affecting the chiroptical properties. Increasing the OA quantity up to 1 μL the stability increases, but for higher concentrations OA enters the perovskite structure, as demonstrated by the stacking distance increase among the inorganic layers detected by XRD, leading to a decrease in the chiroptical response.[36]

In the same year Yan and co-workers investigated the effect of mixing alkyl and aryl cations, obtaining the perovskites $(R/S\text{-MPA})(C_3A)PbBr_4$ and $(R/S\text{-MPA})(C_4A)PbBr_4$, where C_3A = propylammonium and C_4A = butylammonium. The related single crystals present a different crystal structure *vs.* the pure chiral counterpart and crystallize in the $P2_1$ space group. Interestingly, the generated 2D perovskites feature corner-sharing $PbBr_6^{4-}$ 2D layers hydrogen-bonded by an alternance of MPA and C3A or C4A cations (Fig. 16), which are stabilized with the 1 : 1 ligand ratio by (sp^3) CH···π interactions. The authors found out a CD signal of higher amplitude and opposite sign for the MBA/C_4A HOIP *vs.* the pure chiral counterpart, with g_{CD} increasing in modulus and changing in sign from -1.2×10^{-4}

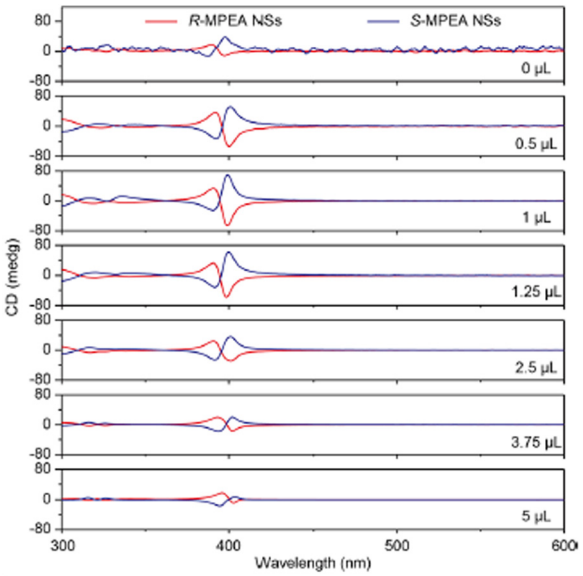

Fig. 15 CD spectra of $(R/S\text{-MPA})_2PbBr_4$ prepared with different OA volumes. Reprinted with permission from ref. 36 Copyright©2021 American Chemical Society.

and 1.3×10^{-4} for $(R\text{-MPA})PbBr_4$ and $(S\text{-MPA})PbBr_4$ to 2.5×10^{-4} and -2.7×10^{-4} for $(R\text{-MPA})(C_4A)PbBr_4$ and $(S\text{-MPA})(C_4A)PbBr_4$. Noteworthy, the title inversion of the CD signal indicates a different CD mechanism passing from pure chiral to mixed chiral/achiral HOIPs, further supported by the different crystal structure in the two cases. However, to confirm this hypothesis further theoretical investigations should be carried out.[37]

In 2023, Lu and colleagues obtained the mixed chiral/achiral HOIPs $(R\text{-MPA}_x\text{PEA}_{(1-x)})_2PbBr_4$ with a nominal x of 0.25, 0.5 and 0.75 and found out a g_{CD} decrease by enhancing the quantity of achiral PEA. Interestingly, this result is opposite to the trends discovered in the same paper for $(R\text{-MBA}_x\text{PEA}_{(1-x)})_2PbBr_4$ and $(R\text{-DMBA}_x\text{PEA}_{(1-x)})_2PbBr_4$ (N-α-dimethylbenzylammonium) and was related to the different steric hindrance around the amino group in the different cases. Indeed, while for *R*-MBA and *R*-DMBA the amino group is close to the phenyl ring and thus sterically hindered, for MPA there is an additional carbon between these two components. Hence, while for *R*-MBA and *R*-DMBA the achiral cation plays a beneficial role in reducing the steric hindrance, in *R*-MPA it does not affect this aspect, only leading to a reduction of chiral molecules content thus decreasing the g_{CD}.[29]

In 2024 Zhang and collaborators doped $(R/S\text{-MPA})_2PbBr_4$ with Mn^{2+} ions, reaching an incorporation of 19%, concentration after which impurities start appearing. As disclosed by XRD, a shrinkage in the unit cell occurs increasing the dopant content, indicating that Mn^{2+} substitutes the Pb^{2+} ions. The authors reported a monotonal increase in both CD intensity and g_{CD} increasing the dopant ratio, occurrence ascribed to the magnetic moment of Mn^{2+}. Noteworthy, the induced magnetic field is rather small as these atoms are isolated, hence do not exhibit a cooperative effect. Measuring the CD of the *R* enantiomer in the presence of a magnetic field the authors unveiled a monotonic increase of intensity with the negative magnetic fields and a sign inversion with the positive magnetic fields (Fig. 17). With this approach the authors were able to in-depth investigate the fine structure quantifying the exciton splitting and Zeeman splitting energy. In line with the CD results, also the CPL increases by increasing of dopant ratio, reaching 11% when the Mn^{2+} amounts is 19%.[38]

HOIPs with 1-(2-naphthyl)ethylammonium (NEA)

Aiming to tune the band-gap over a wide-range region, in 2020 Ahn and co-workers modulated the chiral cations and the halogen atoms, obtaining $(R\text{-MBA})_2PbI_{4(1-x)}Br_{4x}$, whose behaviour is already reported above, and the novel HOIPs $(R/S\text{-NEA})_2PbI_{4(1-y)}Br_{4y}$ with y = 0, 0.3, 0.5, 0.7, and 1.0 (NEA = 1-(2-naphthyl)ethylamine). It must be noted that the authors did not solve its crystal structure but assigned the stoichiometry on the basis of the XRD pattern analogies with the MBA counterpart. By measuring the CD, the authors retrieved an almost flat curve in the fully iodide HOIP and a substantial signal increase over y = 0.3. As witnessed by powder XRD, employing the larger NEA cation, the transition from the iodide determinant phase to the bromide determinant one occurs when y is 0.3. In this case the latter phase is more chiroptically active, leading to a strong CD signal that gradually blue-shifts increasing the bromide content (Fig. 18). Interestingly, the CD intensity of the NEA-based HOIPs is over 60 mdeg, significantly

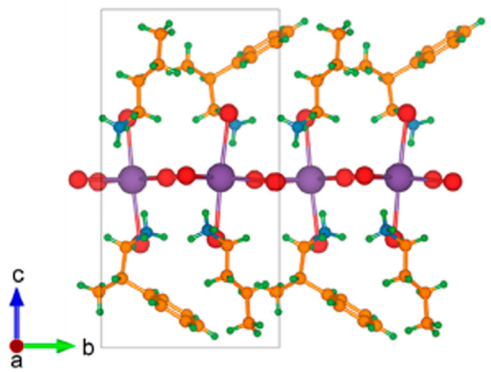

Fig. 16 Crystal structure of $(S\text{-MPA})(C_4A)PbBr_4$, featuring the alternance of *S*-MPA and C_4A cations. Reprinted with permission from ref. 37 Copyright©2021 American Chemical Society.

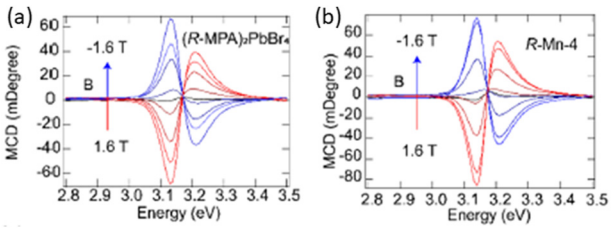

Fig. 17 CD spectra acquired varying the magnetic field from −1.6 to 1.6 T on (a) undoped $(R/S\text{-MPA})_2PbBr_4$ and (b) 19% Mn^{2+} doped $(R/S\text{-MPA})_2PbBr_4$. Reprinted with permission from ref. 38 Copyright©2024 American Chemical Society.

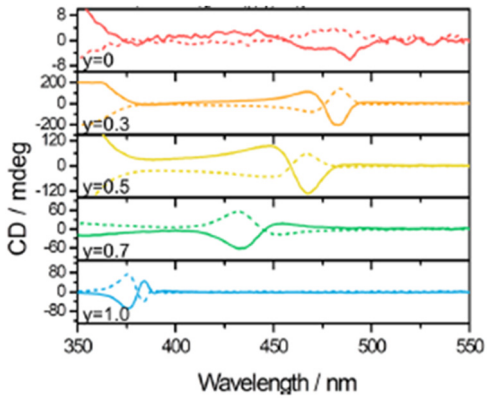

Fig. 18 CD spectra of $(R/S\text{-NEA})_2PbI_{4(1-y)}Br_{4y}$. Reprinted with permission from ref. 23 Copyright©2020 American Chemical Society.

higher the MBA-based ones reported in the same work and associated to a larger magnetic transition dipole moment for the bigger cation.[23]

The single-crystal SC-XRD characterization of the bromide NEA-based HOIP appeared in 2023 with Son and co-workers, who synthesized $(R/S\text{-NEA})_2PbBr_4$ and $(R/S\text{-NPB})_2PbBr_4$ (NPB = 1-(1-naphthyl)ethylamine, which will be discussed below). The authors reported that $(R/S\text{-NEA})_2PbBr_4$ crystallizes in the monoclinic Sohncke space group $P2_1$ and features layers of corner-sharing distorted octahedra separated by the chiral cations (Fig. 19), hydrogen bonded through the amino groups the bromide anions and leading to a *d*-spacing of 20.1 Å.

This distance is lower than the sum of the length of two chiral cations, indicating a mean NH_3^+ penetration depth of *ca.* 0.253 Å. The authors reported the chiroptical characterization of the *R* enantiomer as a representative example. First, from the UV-Vis spectrum the authors reported a bandgap of 3.66 eV, then they observed a bidentate CD signal centred at 382 nm with Cotton effect, leading to a g_{CD} of -2.78×10^{-3}. Moreover, to get rid of a possible overestimation due to rough morphology the authors added 10 mol% of methylammonium bromide as an additive. As evidenced by powder XRD its addition did not induce structural differences, but the final g_{CD} decreased to -9.61×10^{-4}, a value also accounting for the linear dichroism and linear birefringence (LB) effects (collectively called LDLB). The authors also measured the CPL, reporting a g_{CPL} value of -2.14×10^{-3} and a lifetime of few nanoseconds typical of FE emission, and investigated the stability of the title HOIP, observing that it maintains its crystal structure and chiroptical properties up to at least six weeks under environmental conditions and 7 days in harsh conditions (348 K, 75% of relative humidity).[39]

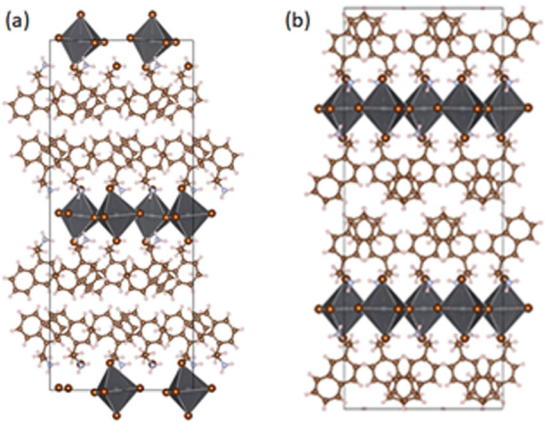

Fig. 19 Crystal structure portion, viewed along the [100] crystallographic direction, of (a) $(S\text{-NEA})_2PbBr_4$ and (b) $(Rac\text{-NEA})_2PbBr_4$. Reprinted with permission from ref. 39 Copyright©2023 Nature Publishing Group.

HOIPs with 1-(1-naphthyl)ethylammonium (NPB)

$(R/S/Rac\text{-NPB})_2PbBr_4$ were firstly reported by Jana and collaborators in 2020 and characterized by SCXRD. The *R* and *S* enantiomers crystallize in the noncentrosymmetric space group $P2_1$ and feature layers of $PbBr_6^{4-}$ corner-sharing octahedra alternated to bilayers of organic cations, resulting in a crystal structure similar to that reported for $(R/S\text{-NEA})_2PbBr_4$. On the contrary, the racemic compound displays an analogue structural motif but adopts the centrosymmetric space group $P2_1/c$, in line with overall symmetrical distortions.[40]

An exhaustive chiroptical characterization was performed by Son *et al.* in a work discussing $(R/S\text{-NPB})_2PbBr_4$ and $(R/S\text{-NEA})_2PbBr_4$ (see above). First, by comparing the *d*-spacing of these two perovskites the authors noticed the occurrence of weaker hydrogen bonds for the NPB-based HOIP, in agreement with its lower melting point disclosed by thermogravimetric and differential scanning calorimetry analysis and a lower stability in harsh conditions. Then, the authors measured the UV-Vis absorption spectrum, reporting a bandgap of 3.57 eV, and the CD signal, featuring a maximum at 393 nm and a g_{CD} of 2.01×10^{-3}, slightly lower than the NEA counterpart, probably because of the lower chirality transfer induced by the weaker hydrogen bonds. This difference is also evidenced in the asymmetry factor of the sample synthesized with 10 mol% of methylammonium bromide, as already explained in the case of NEA, featuring a g_{CD} of -6.84×10^{-4}. This value also reflects in the CPL behaviour (Fig. 20), indicating a slightly lower g_{CPL} value, namely 1.89×10^{-3}.[39]

HOIPs with other chiral cations

In 2022 Fan and co-workers employed the diamine 3-(aminomethyl)-piperidine (3AMP) to synthesize the corresponding 2D perovskite with $(R/S\text{-3AMP})PbBr_4$ stoichiometry. At 298 K the authors found out a DJ crystal structure displaying the chiral $P2_1$ space group and featuring $PbBr_6^{4-}$ octahedra alternated by a monolayer of organic diamines, which employ both the N atoms to form hydrogen bonds with adjacent inorganic layers. Interestingly, the two crystallographically independent 3AMP cations adopt different configurations with different hydrogen interactions, thus contributing to an enhanced octahedral distortion. Notably, at high temperature the title HOIP undergoes an order–disorder transition from a ferroelectric phase to a paraelectric one, whose crystal structure was solved at 405 K. The material crystallized in the *P*422 chiral space group and

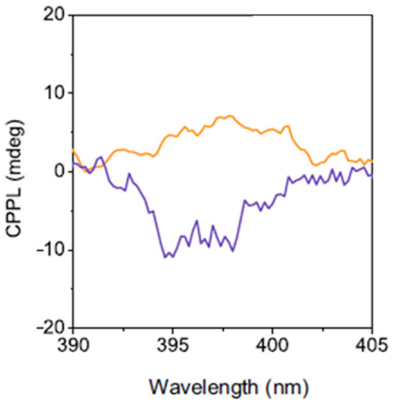

Fig. 20 CPL spectra of $(R\text{-NPB})_2PbBr_4$ (orange curve) and $(R\text{-NEA})_2PbBr_4$ (violet curve). Reprinted with permission from ref. 39 Copyright©2023 Nature Publishing Group.

displays a significantly low octahedra distortion. The authors carried out the chiroptical characterization on the RT phase by means of UV-Vis absorption, observing a sharp absorption at 430 nm and a broad band at *ca.* 450 nm with a bandgap of 2.78 eV. They then measured the CD observing mirrored curves for the two enantiomers (Fig. 21), with several peaks and Cotton effect, and calculated the g_{CD} as 1.8×10^{-3}. In addition, a featureless curve was observed for the racemic sample.[41]

As already discussed in the previous sections, *R*-N-DMBA was employed to study the effect of mixing chiral and achiral cations, showing for *R*-MBA and *R*-N-DMBA an increase in g_{CD} by inserting achiral cations due to a reduction of the steric hindrance. Interesting, for *R*-N-DMBA, whose steric hindrance is higher than that of *R*-MBA, only a moderated g_{CD} enhancement is observed (Fig. 22), requiring a composition equal to a PEA/N-DMBA nominal ratio of 75% to reach the value of $g_{CD} = 4.9 \times 10^{-4}$.[29]

Lead-free 2D HOIPs

As an alternative to the toxic Pb^{2+}, Sn^{2+} was employed in 2020 by Lu and collaborators to synthesize $(R/S/Rac\text{-MBA})_2SnI_4$,

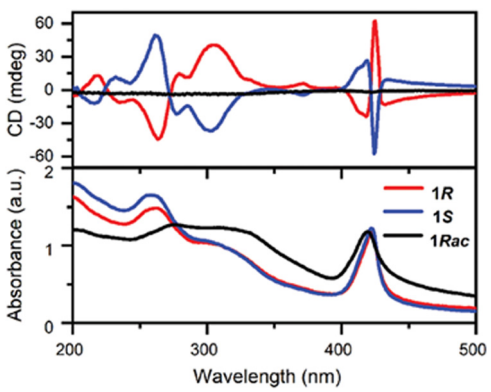

Fig. 21 CD spectra of $(R/S/Rac\text{-3AMP})PbBr_4$ (above) along with their absorption spectra (below). Reprinted with permission from ref. 41 Copyright©2022 Wiley-VCH GmbH.

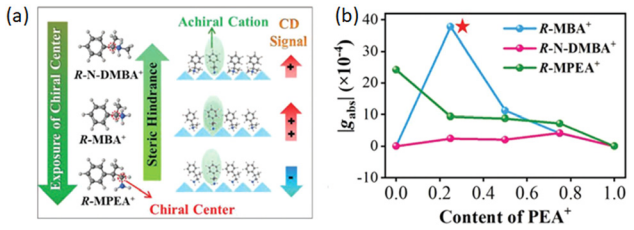

Fig. 22 (a) Schematic illustration of the chiral cations and of their behaviour as a consequence of the PEA content. (b) g_{CD} behaviour as a function of the PEA content. Reprinted with permission from ref. 29 Copyright©2022 Wiley-VCH GmbH.

featuring the similar 2D structural motif of the lead-based counterparts. The two enantiomers crystallize in the chiral $P2_12_12_1$ space group while the racemic in the *Pnma* centrosymmetric one. Interestingly, all the compounds display significantly distorted octahedra, with a distortion index (*D*) value of 79×10^{-3} for the two enantiomers and 76×10^{-3} for the racemic, values substantially higher than those of $(R/S/Rac\text{-MBA})_2PbI_4$ (22×10^{-3} and 14×10^{-3} for the enantiomers and the racemic, respectively) and of other achiral Sn–I layered perovskites (Fig. 23). All the compounds feature similar absorption spectra, with a peak at 408 nm and a shoulder at 452 nm resulting in a bandgap of 2.5 eV.

The CD measurements disclosed mirrored curves with peaks at 357, 402, 443, and 473 nm with Cotton effect near the bandedge electronic transition. The authors then synthesized the solid solutions $(R/S\text{-MBA})_2Pb_{1-x}Sn_xI_4$, with *x* varying from 0 to 1, and observed a bandgap bowing in the alloyed sample, where the end members feature the highest values. They attributed this occurrence to an energy mismatch between the s and p orbitals of Pb^{2+} and Sn^{2+} that affects the band structure of the various compounds, as supported by DFT calculations. The CD response was also measured for the various compositions unveiling a disappearance of the derivative peaks near the bandedge, and an interesting trend of the second lowest energy peak in line with the bandgap bowing. Indeed, increasing the Sn^{2+} concentration from 0 to 50% it red-shifts from 380 to 466 nm, then it blue-shifts to *ca.* 440 nm.[42]

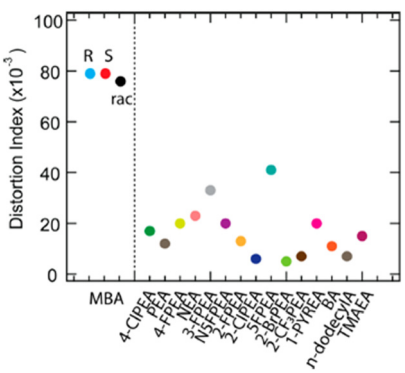

Fig. 23 *D* values of $(R/S/Rac\text{-MBA})_2SnI_4$ and of other Sn–I layered HOIPs reported in the literature. Reprinted with permission from ref. 42 Copyright©2020 American Chemical Society.

In 2024 our group synthesized (*R*/*S*/*Rac*-4-Cl-MBA)$_2$SnI$_4$, as the halogen in *para* position is known to induce further weak interactions in the HOIPs. The single crystal structures were disclosed by SC-XRD: the two enantiomers adopt the triclinic *P*1 chiral space group while the racemic crystallizes in the centrosymmetric *Pnma*, and all the materials feature the already detailed 2D structural motif. The *D* values of (*R*/*S*-4-Cl-MBA)$_2$SnI$_4$ is about half of that of (*R*/*S*-MBA)$_2$SnI$_4$, namely 40 × 10^{-3}, although significantly higher than the (*R*/*S*-MBA)$_2$PbI$_4$. Noteworthy, also the lead-based counterpart displayed a diminishing of the distortion index passing from MBA to 4-Cl-MBA. The UV-Vis absorption spectra feature steep optical band edges around 600 nm and a slight red-shift for the racemic (Fig. 24a), values turning into a bandgap of 2.12 for the *R* and *S* enantiomers and 2.08 for the racemic. Interestingly, these values are among the lowest bandgap ever reported for a chiral 2D HOIP. The CD spectra indicated two peaks, at about 465 and 520 nm, with opposite sign for the two enantiomers, as well as the characteristic Cotton effect and a g_{CD} of 1 × 10^{-4} (Fig. 24b). Moreover, the PL spectra displayed a minor tail close to the absorption edge and a broad peak at *ca.* 730 nm, thus featuring a substantial Stokes shift, with STE characteristics (Fig. 24c). This result, not observed in the lead-based counterparts, was ascribed to the high distortion index of the octahedra and could be an advantage for practical applications. Moreover, considering the left- and right-handed contributions to the PL, a g_{CPL} value of *ca.* 0.02 was obtained at 90 K (Fig. 24d).[43]

Another alternative to the toxic lead is Cu^{2+}, which was employed by Sun and colleagues in 2020 to evaluate the chiroptical properties of the corresponding perovskite (*R*/*S*/*Rac*-MPA)$_2$CuCl$_4$. As unveiled by SC-XRD structural determination, the two enantiomers are antisymmetrically isostructural and crystallize in the chiral *C*2 space group, featuring $CuCl_6^{4-}$ octahedra separated by a bilayer of organic cations. Notably, the

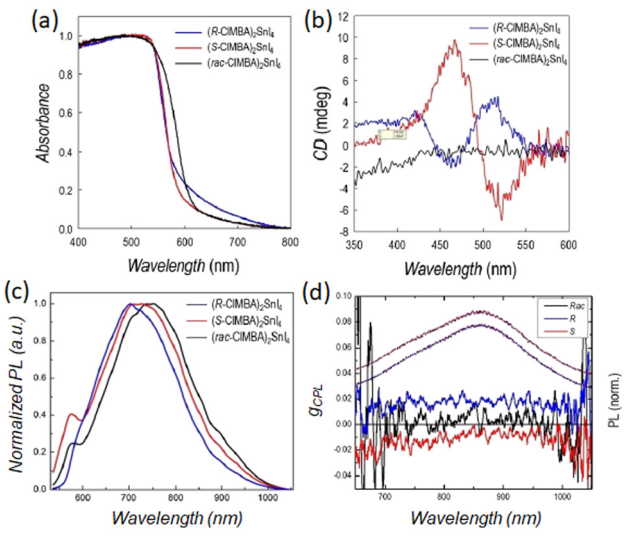

Fig. 24 (a) Absorbance; (b) CD, and (c) μPL spectra of (*R*/*S*/*Rac*-ClMBA)$_2$SnI$_4$. (d) g_{CPL} (left axis) and static PL (right axis) for (*R*/*S*/*Rac*-ClMBA)$_2$SnI$_4$ measured at 90 K. Reprinted with permission from ref. 43 Copyright©2024 Wiley-VCH GmbH.

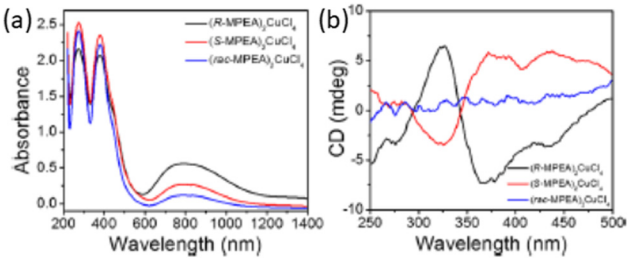

Fig. 25 (a) UV-Vis absorption spectra and (b) CD spectra of (*R*/*S*/*Rac*-MPA)$_2$CuCl$_4$. Reprinted with permission from ref. 44 Copyright©2020 American Chemical Society.

octahedra display a substantial distortion which was attributed to the Jahn–Teller effect commonly displayed by copper ions. The UV-Vis-NIR absorption spectra of the three compounds are nearly identical, featuring an absorption peak at *ca.* 379 nm related to the HOIPs excitonic feature (Fig. 25a). In addition, the broad band centred at *ca.* 800 nm is indicative of the Laporte forbidden Cu^{2+} d–d transitions. The authors reported the CD spectra of the two enantiomers, unveiling strong and opposite CD signals with maxima at 324, 372 and 436 nm, and of the racemic which is featureless as expected (Fig. 25b). Interestingly, all the peaks are located before the absorption edge at 567 nm, index of a spin degeneracy lifting within the band edge electronic states ingenerated by the chiral cations.[44]

In 2022 Yu *et al.* employed 3-aminopyrrolidine to synthesize the double perovskites (*R*/*S*-3AP)$_4$AgBiBr$_{12}$, whose crystal structure was characterized by SCXRD. The authors reported that the two compounds crystallize in the *P*1 space group, where layers of alternated corner-sharing [AgBr$_6$] and [BiBr$_6$] octahedra are separated by bilayers of organic cations, the latter divided by additional bromide anions interacting with the exocyclic amino group, not engaged in hydrogen bonds with the metal-halide octahedra (Fig. 26). UV-Vis absorption spectra indicated a peak with maximum at *ca.* 400 nm, resulting in a bandgap of 2.6 eV in accordance with the theoretical calculations. Moreover, the CD featured peaks at the same positions with opposite values, indicating a transfer chirality from the organic molecules to the HOIP structure, while a rather flat signal for the racemic compound.[45]

Quasi-2D HOIPs

In addition to the chiroptical characterization as a pure 2D phase, the archetypal (*R*/*S*-MBA)$_2$PbI$_4$ was investigated in form of quasi-2D crystals. Indeed, in 2022 Dayan and co-workers mixed APbI$_3$, where A is MA^+ or a mixture of Cs^+ and FA^+, with the title 2D HOIP with different ratios, obtaining materials with different *n* spanning from the pure 2D to the pure 3D. By measuring the CD, the authors observed that a more pronounced chirality is observed at low ⟨*n*⟩, as expected from the higher quantity of chiral molecules. Accordingly, also g_{CD} gradually enhances going from 3D to 2D, being an order of magnitude higher at ⟨*n*⟩ = 2, which is the lower n value measured.[46]

In the same year Yang and collaborators carried out a similar investigation on the bromide counterpart, synthesizing

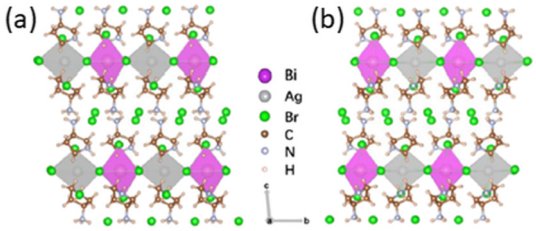

Fig. 26 Crystal structure portion of (a) $(S\text{-3AP})_4AgBiBr_{12}$ and (b) $(R\text{-3AP})_4AgBiBr_{12}$. Reprinted with permission from ref. 45 Copyright©2022 American Chemical Society.

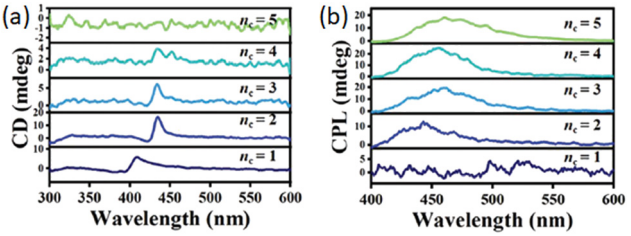

Fig. 28 (a) CD and (b) CPL spectra of $(S/R\text{-MBA})_2MA_{n-1}Pb_nBr_{3n+1}$ as a function of $\langle n \rangle$. Reprinted with permission from ref. 48 Copyright©2022 Wiley-VCH GmbH.

HOIPs with formula $(R/S/Rac\text{-MBA})_2(CsMA)_{n-1}Pb_nBr_{3n+1}$, varying $\langle n \rangle$ from 1 (pure 2D) to higher values. The authors reported that all the chiral materials are CD active, whereas the racemic displays a featureless signal. As already observed in the iodide HOIPs, g_{CD} diminishes as $\langle n \rangle$ increases as a consequence of the minor content of chiral cations. The authors measured the CPL unveiling that while the pure 2D material does not emit, the HOIPs with $\langle n \rangle$ = 2, 3 and 4 present mirror-like features from 450 to 600 nm (Fig. 27), and the g_{CPL} diminishes as $\langle n \rangle$ enhances. Moreover, the authors measured the CD upon generating and varying a magnetic field, observing that g_{CPL} changed on the basis of its magnitude and direction.[47]

In 2023, Wen *et al.* employed polyacrylonitrile (PAN) to encapsulate nanofiber films of quasi-2D perovskite nanosheets of formula $(S/R\text{-MBA})_2MA_{n-1}Pb_nBr_{3n+1}$ ($\langle n \rangle$ = 1, 2,...,5) and investigated the blue-emissive CPL performance at room temperature. The authors confirmed the trend already reported for the CD, *i.e.* a signal decrease from n = 2 to n = 5. However, with n = 1 the signal is lower probably because of the weaker stability of the pure 2D HOIPs upon polymer incapsulation. The authors measured the CD (Fig. 28a) obtaining a g_{CD} value of 7.5×10^{-4} for the *S* enantiomer with $\langle n \rangle$ = 2. They then focused on the CPL (Fig. 28b), observing that, while the pure 2D material is silent, the other material feature a broad CPL, whose maximum shifts from *ca.* 440 nm to *ca.* 460 nm increasing $\langle n \rangle$ from 2 to 5. Moreover, the higher g_{CPL} value is retrieved for $(R\text{-MBA})_2MAPb_2Br_7$ and corresponds to -8×10^{-3}.[48]

In the same year Cao and collaborators focused on the effect of changing the inorganic layers thickness in MPA-based HOIPs, namely $(S/R\text{-MPA})_2Cs_{n-1}Pb_nBr_{3n+1}$ with $\langle n \rangle$ = 1, 2 and 3. The authors reported a strong CD signal at the first exciton peak position, which red-shifts to lower energies while increasing $\langle n \rangle$, in line with the bandgap change. A decrease in the signal intensity along with a reduction in the Cotton effect and a diminution of the g_{CD} is retrieved increasing the layer thickness, although the g_{CD} values remain in the order of 10^{-4} (Fig. 29a). Similarly the CPL emission red-shifted with higher $\langle n \rangle$, featuring a substantial diminution of the g_{CPL}, which passes from 2.3×10^{-3} in to 7×10^{-5} from $\langle n \rangle$ = 1 to $\langle n \rangle$ = 3 (Fig. 29b).[49]

Quasi-2D HOIPs with NEA were reported in 2022 by Liu and colleagues who synthesized $(NEA)_2(MA)_{n-1}Pb_nI_{3n+1}$ with various $\langle n \rangle$ varying from 1 to 5. The authors reported a CD signal decreasing with increasing $\langle n \rangle$, with maxima of −178 and 244 mdeg for the *R* and *S* enantiomers with $\langle n \rangle$ = 1, 98 and −52 for the quasi-2D enantiomers with $\langle n \rangle$ = 2, and a signal of less than 5 mdeg for $\langle n \rangle$ = 5. The authors then calculated g_{CD} for the HOIPs with $\langle n \rangle$ equal to 1 and 2, reporting that the induced chiroptical activity is roughly the same (Fig. 30).[50]

Yao and co-workers in 2024 synthesized the NPB-based quasi 2D perovskite with $(R/S\text{-NPB})_2(FA_xCs_{1-x})_{n-1}Pb_nBr_{3n+1}$ stoichiometry and focused on tuning the composition of the achiral cation, unveiling that the best performing composition is attained when $\langle n \rangle$ is 3 and x is 0.85. The authors reported that the PLQY is significantly enhanced to 91.0% upon substituting FA^+ with 15% of Cs^+, while the PLQY of the fully FA^+-based HOIP is 67.5%. The CD spectra of $(R/S\text{-NPB})_2(FA_{0.85}Cs_{0.15})_2Pb_3Br_{10}$ enantiomers feature symmetric curves, with a g_{CD} of *ca.* 2×10^{-4}. The authors then disclosed that the PL emission, attributable to the 3D phase, is circularly polarized, and calculated g_{CPL} as a function of the Cs^+ content, unveiling that it decreases from 8.6×10^{-2} in the fully FA^+ HOIP to 6.8×10^{-2} in the 15% Cs^+

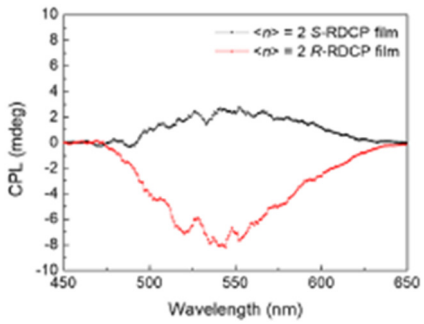

Fig. 27 CPL spectra of $(R/S/Rac\text{-MBA})_2(CsMA)Pb_2Br_7$. Reprinted with permission from ref. 47 Copyright©2022 American Chemical Society.

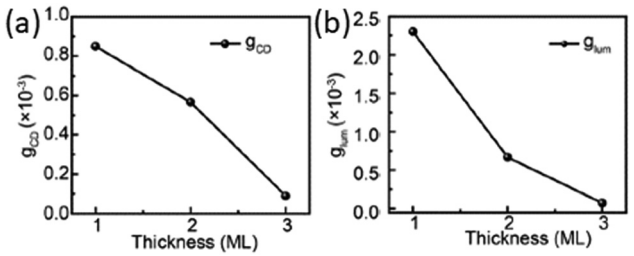

Fig. 29 (a) g_{CD} and (b) g_{CPL} of $(S/R\text{-MPA})_2Cs_{n-1}Pb_nBr_{3n+1}$ as a function of the layer thickness $\langle n \rangle$. Reprinted with permission from ref. 49 Copyright©2023 Wiley-VCH GmbH.

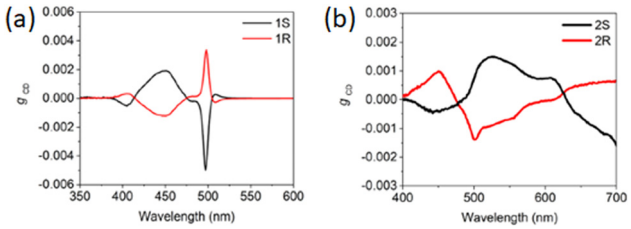

Fig. 30 g_{CD} of $(NEA)_2(MA)_{n-1}Pb_nI_{3n+1}$ with (a) $\langle n \rangle$ = 1 and (b) $\langle n \rangle$ = 2. Reprinted with permission from ref. 50 Copyright©2022 American Chemical Society.

one. They also investigated the CPL as a function of the temperature for $(R\text{-NPB})_2(FA)_2Pb_3Br_{10}$, from 80 to 300 K, unveiling a monotonous g_{CPL} decrease with the temperature increase, an indication that the latter induces a decrease of the 3D phase spin polarization.[51]

Application of chiral 2D HOIPs

As expected, $(R/S\text{-MBA})_2PbI_4$ has been the most investigated HOIP even from the applicative viewpoint, displaying promising use in the fields of CPL and X-ray photodetection, spin-LED, energy harvesting devices, as well as photocatalysis. In addition, several works appeared employing MPA, NEA and NPB which are, after NPB, the most commonly investigated chiral cations in the construction of HOIPs.

$(R/S\text{-MBA})_2PbI_4$ was used as a single crystalline 2D phase to build up a Stokes photodetector by Zhao *et al.*, who synthesized it in form of nanowires (Fig. 31) with a subwavelength width dimension, featuring single crystallinity as well as a pure crystallographic orientation, characteristics that allowed for an efficient in-plane carrier transport. The authors reported a good photoresponse for both circularly and linearly polarized light, a responsivity of 47.1 A W^{-1} and a detectivity of 1.24×10^{13} Jones, highlighting the possibility of employing these nanowires in integrated imaging devices due to the easiness of their fabrication.[52]

Yuan *et al.* found out that the Cl-substituted HOIP $(R\text{-4-Cl-MBA})_2PbI_4$, possessing a reduced lattice distortion and

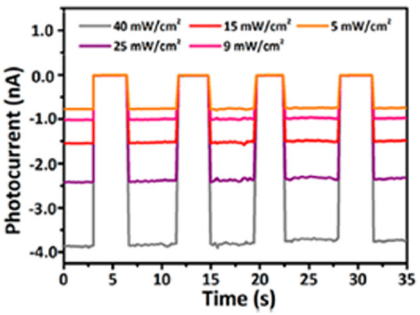

Fig. 32 Photocurrent densities at various incident light intensities of the $MAPbI_3/(R\text{-4-Br-MBA})_2PbI_4$ device at 785 nm under zero bias. Reprinted with permission from ref. 55 Copyright©2021 American Chemical Society.

enhanced halogen–halogen interactions *vs.* the unsubstituted perovskite, behaves as a high-performance CPL photodetector, thanks to a stiffer lattice and a weaker electron–phonon coupling. Indeed, these characteristics increase carrier transport and thermal stability and impart an anisotropy factor of 0.25, a responsivity surpassing 95.7 ± 9.3 A W^{-1} and a detectivity as high as $(3.05 \pm 0.30) \times 10^{13}$ Jones.[53] Similarly, $(R\text{-4-Br-MBA})_2PbI_4$ displays an elevated vis-NIR dual-modal CPL-sensitive direct detecting performance upon irradiation with both visible light (520 nm) and NIR light (800 nm), with the on/off current ratios (I_{ON}/I_{OFF}) in the order of 10^3, and anisotropy factors for photocurrent higher than 0.1.[54] In another work, an heterostructure composed of $MAPbI_3$ and $(R\text{-4-Br-MBA})_2PbI_4$ enabled the attainment of a self-powered CPL detector with an anisotropy factor for the photocurrent of 0.25, an outstanding I_{ON}/I_{OFF} of *ca.* 10^5 (Fig. 32) and a detectivity of *ca.* 10^{10} Jones.[55]

Cao and collaborators coupled $(R/S\text{-MBA})_2PbI_4$ with black phosporous, a class of materials already employed in photodetection. Interestingly, the authors found out that the heterostructure increased the performance and enriched the functionalities of BP alone, favoring an improvement of carrier mobility, photoresponsivity, and polarization sensitivity. In particular, the photodetector responsivity and photogain of black phosporous are enhanced by almost one order of magnitude in the heterostructure, especially upon exciting above the bandgap of perovskite. Moreover, while black phosporous

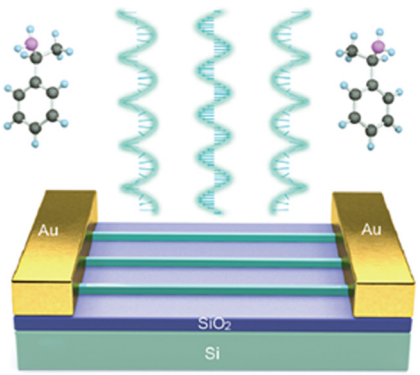

Fig. 31 Schematic illustration of the Stokes photodetector. Reprinted with permission from ref. 52 Copyright©2021 American Chemical Society.

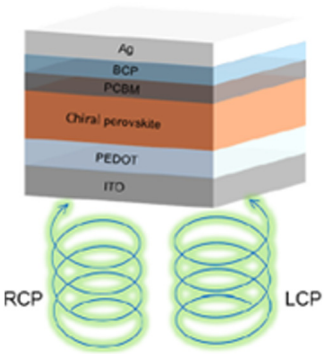

Fig. 33 Schematic representation of the photodiode structure. Reprinted with permission from ref. 57 Copyright©2023 American Chemical Society.

display good responses only at positive gate voltages, the title heterostructure behaves in the same manner with positive and negative voltages.[56] Yao and co-workers incorporated the mixed tin-lead $(R/S\text{-MBA})_2Pb_{1-x}Sn_xI_4$ into a photodiode structure composed as ITO/PEDOT/chiral HOIP/PCBM/BCP/Ag (Fig. 33) to achieve CPL detection. The authors discovered a linear increment of the photocurrent and responsivity with light intensity variation from 0.005 to 20 mW cm^{-2}, thus the absence of any remarkable decrease of response with the light intensity enhancement. Peak responsivity of 0.14 A W^{-1} was achieved for the device built up employing $(S\text{-MBA})_2Pb_{0.9}Sn_{0.1}I_4$ without bias. The authors then found out a specific detectivity of 1.63×10^{11} Jones, in line with the values reported for chiral HOIPs photodetectors. Interestingly, an asymmetry factor for the photocurrent of 0.44 was achieved, a significantly higher value compared to the 2D Pb-based HOIPs.[57]

Tao and colleagues fabricated a type I heterostructure by coupling $MAPbI_3$ with $(R\text{-MBA})_2PbI_4$, thus synthesizing the relative quasi-2D HOIP, and reported that this facilitates the energy funneling from the chiral-2D phase to the 3D conductive channel, enhancing the charge transport features (Fig. 34). Indeed, it is known that the insulating organic cations in 2D HOIPs generally hinder carrier transport and charge extraction, resulting in a reduced responsivity of photodetectors. The prepared device exhibits an anisotropy factor of 0.13 and a high specific detectivity of 6.8×10^{10} Jones, significantly higher than those based on fully 2D perovskites.[58]

Intriguingly, the MPA cation was employed in the form of the quasi-2D HOIP $(R\text{-MPA})_2MAPb_2I_7$ for the photodetection of polarized light in 2020,[59] and further heightened in 2021 by coupling the title phase with the 3D counterpart $MAPbI_3$, favouring the charge transfer process (Fig. 35) and reaching an asymmetry factor of 0.67, significantly higher than the $n = 2$ counterpart (0.1). Moreover, a responsivity of 1.2 mA W^{-1} under an incident light density of 0.2 mW cm^{-2} was achieved, along with an external quantum yield (EQE) of 2.8% and a detectivity value of 1.1×10^{12} Jones.[60]

A lead-free photodetector was then created in 2022 employing the chiral perovskite $(R/S\text{-MPA})_4AgBiI_8$, attaining an outstanding responsivity of 52 mA W^{-1} and a detectivity exceeding 3.9×10^{11} Jones.

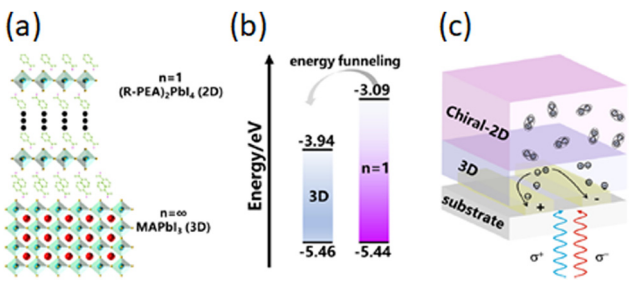

Fig. 34 (a) 2D/3D HOIP-based heterojunction; (b) related energy band diagram; (c) working mechanism of the related CPL photodetector. Reprinted with permission from ref. 58 Copyright©2023 Royal Society of Chemistry.

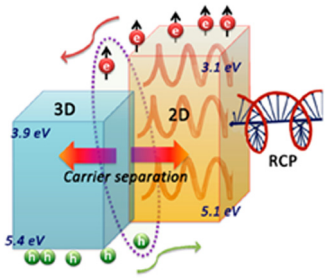

Fig. 35 Pictorial representation of the band alignment of the HOIP heterostructure along with the photogenerated carrier mobility. Reprinted with permission from ref. 60 Copyright©2021 American Chemical Society.

In 2023 Zhao and colleagues successfully created an heterojunction between 2D and quasi-2D HOIPs, namely $(R/S\text{-MPA}]_2MA_{n-1}Pb_nI_{3n+1}$ with $n = 1$ and $n = 2$, in forms of nanowire arrays, attaining a photodetector featuring an outstanding responsivity of 22.14 A W^{-1}, an anisotropy factor of 0.38 and a polarized ratio of 1.5.[61]

The NEA cation was also utilized in photodetectors, for example by Liu and co-workers who prepared $(R/S\text{-NEA})_2(MA)_{n-1}Pb_nI_{3n+1}$ with n varying from 1 to 5, reporting that the responsivity increased with n, with a maximum value of 15.7 A W^{-1}, and a dissymmetry factor of 0.15.[50]

Finally, a photodetector with a diamine was reported taking advantage of the chiral $(R\text{-3AMP})PbBr_4$, obtaining a device showing a I_{ON}–I_{OFF} ratio of 5.8×10^3 (Fig. 36a), a responsivity of 41.9 mA W^{-1} and a specific detectivity of 2.4×10^{12} Jones (Fig. 36b).[41]

With a slightly different aim, Wu and collaborators took advantage of the chirality induced photovoltaic effect to realize a self-powered X-ray detector based on $(R\text{-MPA})_4AgBiI_8$. Indeed, the spontaneous electric polarization yield a polar photovoltage of 0.36 V, enabling the separation and transport of X-ray-produced carriers, thus allowing for the self-powered detection. The material featured a sensitivity of 46.3 μC Gy^{-1} cm^{-2} and a detection limit of 85 nGy s^{-1} at zero bias. Moreover, applying a 50 V bias the sensitivity can be enhanced to 949.6 μC Gy^{-1} cm^{-2}.[62]

Regarding MBA, Guan and co-workers built up a self-driven X-ray detector based on the quasi-2D HOIP $(S\text{-4-Br-MBA})_2FAPb_2I_7$, displaying a radiation photovoltaic of 0.85 V, a sensitivity of 87.8 μC Gy_{air}^{-1} cm^{-2} and a detection limit low to 161 nGy_{air} s^{-1}.[63]

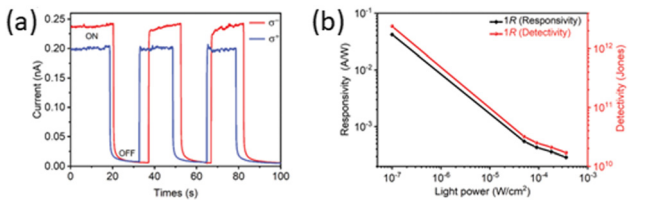

Fig. 36 (a) Photocurrent during L- and R-CPL irradiation at 430 nm and (b) responsivity and detectivity *vs.* power intensity at 430 nm of $(R\text{-3AMP})PbBr_4$. Reprinted with permission from ref. 41 Copyright©2022 Wiley-VCH GmbH.

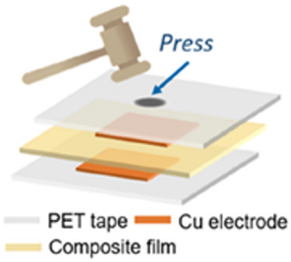

Fig. 37 Schematic representation of the energy harvesting device architecture. Reprinted with permission from ref. 64 Copyright©2023 American Chemical Society.

Energy harvesting devices were constructed by employing the $(R/S\text{-4-Br-MBA})_2PbI_4$, unveiling that their composite films (Fig. 37) can be utilized to generate voltages and currents up to *ca.* 0.6 V and *ca.* 1.5 μA, respectively, upon periodic impacting with a force of 2 N.[64]

$(R/S\text{-MBA})_2PbI_4$ was also coupled with other materials, such as transition metal dichalcogenides, to manipulate the valley polarization without the employment of circularly polarized light excitation, at relatively mild temperatures (200 K) and avoiding the use of external magnetic field, hence promoting the development of HOIP-based spintronic and valleytronic devices.[65]

Moreover, the title HOIP was also employed in heterostructures with CdSe/ZnS quantum dots, taking advantage of the CISS effect to transfer the chirality from the 2D perovskite to the quantum dots and creating spin-LEDs. To this aim, a device with architecture ITO/PEDOT:PSS/TFB/$(R/S\text{-MBA}_2PbI_4)$ was realized (Fig. 38). Interestingly, $(R/S\text{-MBA})_2PbI_4$ imparts a spin injection polarization higher than 80% allowing for a CP-EL asymmetric factor ($g_{CP\text{-}EL}$) as high as 1.6×10^{-2}.[66]

Spin-LEDs were also constructed with quasi-2D HOIPs, for example in the work reported by Kim and co-workers where they built up a ITO/*m*-PEDOT:PSS/$(S\text{-MBA})_2PbI_4/CsPbI_3$ device and obtained a 2.6% of CP-EL at room temperature.[67]

In a similar approach, Zhang and colleagues mixed chiral MBA and achiral *tert*-butylammonium to obtain the quasi-2D HOIP consisting in the achiral $n = 2$ quantum well and the chiral $n = 1$ one. By creating a type II interface which allows spin selectivity through the CISS effect, the authors attained a $g_{CP\text{-}EL}$ of 10.3% and an EQE of 3.6%.[68]

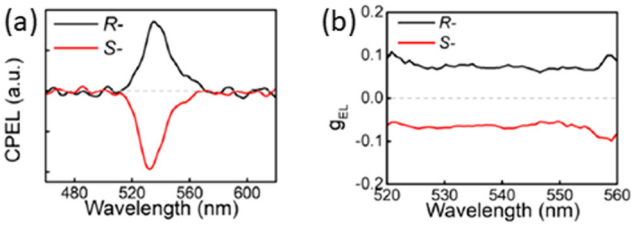

Fig. 39 (a) CPEL spectra and (b) and g_{EL} of spin-LEDs based on $(R\text{-NPB})_2(FA_{0.85}Cs_{0.15})_2Pb_3Br_{10}$. Reprinted with permission from ref. 51 Copyright©2024 American Chemical Society.

Yang *et al.* then employed NEA and the achiral PEA to attain a spin-LED with an HOIP having composition $(PEA_xNEA_{1-x})_2MA_{n-1}PbnI_{3n+1}$, with a PEA : NEA ratio of 1 : 6, which was incorporated in a device composed as ITO/PEDOT:PSS/S/R-NBCP film/TPBi/LiF/Al, where ITO and LiF/Al were utilized as the anode and cathode, respectively. The authors reported an EQE of 3.7% and a maximum g_{EL} of 4.0×10^{-3}.[69] In 2024 Jang and co-workers created a core–shell QDs where the core is $CsPbBr_3$ and the shell is the 2D lead-based bromide HOIP with *R*/*S*-NEA, and employing a device similar to the above described one achieved an EQE of 5.47% and a $g_{CP\text{-}EL}$ of 12% at room temperature.[70]

Yao and collaborators fabricated a spin-LED with promising performances using the chiral NPB and fabricating the quasi-2D $(R/S\text{-NPB})_2(FA_{0.85}Cs_{0.15})_2Pb_3Br_{10}$, which once incorporated into a device yielded a g_{EL} of 7.8×10^{-2} (Fig. 39) and a maximum EQE of 13.5% at room temperature.[51]

Another interesting result came from the $(L\text{-PME}_xPEA_{1-x})_2Cs_{n-1}Pb_n(Cl_yBr_{1-y})_{3n+1}$ (L-PME = L-phenylalanine methyl ester), where the authors investigated the variation of the composition, in particular of the L-PMe ratio, for the construction of a perovskite LED. The authors found out that the constructed device possessed an EQE of 12.43% at 1000 cd m^{-2} and an outstanding power efficiency of 18.42 lm W^{-1}.[71]

The CISS effect induced by $(S\text{-MBA})_2PbI_4$ was also employed to enable efficient spin-dependent oxygen evolution reaction by placing the chiral perovskite as a spin-filtering layer on the photoanode. The constructed water-splitting device, displaying a $NiFeO_x/TiO_2/PTAA/(S\text{-MBA})_2PbI_4/Mo{:}BiVO_4/SnO_2/ITO$ architecture

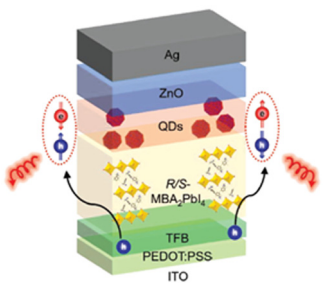

Fig. 38 Pictorical representation of the CISS charge injection for CP-EL emission in the spin-LED device. Reprinted with permission from ref. 66 Copyright©2023 Wiley-VCH GmbH.

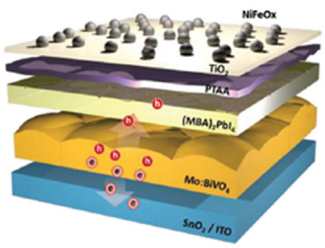

Fig. 40 Pictorial representation, along with the hole transport mechanism, of the oxygen evolution reaction device. Reprinted with permission from ref. 72 Copyright©2023 Wiley-VCH GmbH.

(Fig. 40), showed an outstanding oxygen evolution performance with an overpotential as small as 0.14 V, elevated fill factor, and 230% enhanced photocurrent *vs.* a device without a spin-filtering layer. This device also achieved an elevated operational stability by sustaining *ca.* 90% of the initial photocurrent even after 10 h.[72]

(*R*/*S*-MBA)$_2$PbI$_4$ was also employed as a photocatalyst for the methyl-orange degradation, being able to completely degrade, in 5 minutes, a 30 mg L^{-1} of dye solution, making this HOIP one of the most efficient catalysts for this peculiar reaction.[73] Moreover, MBA/CsPbBr$_3$ nanocrystals were reported as photocatalysts for the asymmetric organic synthesis of N–C axially chiral N-heterocycles, being able to produce *N*-arylindoles with outstanding enantioselectivity, up to 99% ee, upon visible-light excitation at room temperature. By performing DFT calculations the authors indicated that such result is dictated by the discriminated binding of prochiral *N*-arylamine substrates to the NC surface.[74]

It is worth noticing that achiral 2D and quasi-2D perovskites have been widely employed in the field of photoelectrical devices applications. For example, Zhuang and co-workers in 2023 synthesized a device based on a 2D perovskite featuring alternating cations in the interlayer space achieving an outstanding power conversion efficiency (PCE) of 24.58%,[75] while Li and collaborators engineered a 2D/3D heterojunction leading to a PCE of 25.12% at a laboratory scale and of 22.48% in a larger area, namely 1 cm^2.[76] Moreover, in 2024 Gong *et al.* achieved a PCE of 26.03% in a perovskite solar cell (PSC) by utilizing a silver coordination-induced n-doping of [6,6]-phenyl-C$_{61}$-butyric acid methyl ester (PCBM) to prevent the Ag electrode from corrosion and impede iodine migration within the PSC.[77] With these examples, we aim to underline the promising performances of perovskites in a field as important as the one of photoelectrical devices applications, suggesting that investigations employing chiral 2D and quasi-2D HOIPs would be of great interest for breakthrough advancements, as the spontaneous electric polarization induced by the noncentrosymmetric nature could enhance the carrier generation and transport.

Conclusions and outlook

In summary, we reported an overview of the state-of-the-art chiral 2D and quasi-2D HOIPs with a specific correlation between chemical composition, crystal structure and chiroptical properties. Although the field is relatively young, substantial progresses have been made and the number of investigated phases is constantly increasing. Great efforts have been carried out to unveil the role of the chiral cations on the chiroptical properties, aiming at rationalizing the influence of steric hindrance and hydrogen bonding network on the chiroptical response. It is worth noticing, however, that the majority of the chiral molecules employed so far are those commercially available, limiting an in-depth investigation of the parameters concurring to the functional properties. For example, only the modulation of the halogen atoms on the phenyl ring of MBA is reported, to the best of our knowledge, but it would be highly desirable that a similar investigation for cations displaying a different steric hindrance would be realized to advance the understanding of the ligand role from an electron-donating or -attracting viewpoint. In addition, also the solvent could play an important role on the phase purity and defects density, influencing the chiroptical response of the prepared materials. However, this aspect has been taken into consideration only for MBA and with two solvents, namely DMF and ACN. It is indeed of undoubted interest to expand this investigation to other HOIPs and other solvents, including chiral ones as well. The study of chiral perovskites and perovskite derivatives is also quickly moving in the direction of lead-free materials to get rid of the toxic lead, with examples of perovskites investigated from the chiroptical viewpoint containing tin, copper or silver and bismuth. Further progresses in this direction are of great importance, not only because of the lead toxicity issues but also to understand the role of the metal center on the optical properties. For example, from the few reported works it comes out that Sn-containing HOIPs present large distortion indexes, which is a key factor in dictating the chiroptical behaviour. Based on this, we propose that a more systematic study of such a structural-functional relationship would be beneficial for the research area.

In parallel to the characterization of new phases, the research area is also moving from the pure 2D HOIPs to the quasi-2D ones, allowing to couple the advantages of both these two kinds of phases and to further modulate the optical response. This approach turned out to be particularly interesting from the applicative perspective, allowing for the construction of devices with superior performances. Indeed, chiral 2D and quasi-2D HOIPs have been tested in various device types, such as CPL and X-ray photodetection, spin-LED applications, energy harvesting and photocatalysis, highlighting encouraging alternatives to the currently employed technologies. Moreover, we propose that further cutting-edge applications may take advantage of chiral perovskites, not only in virtue of their chiroptical and spin properties but also because of the spontaneous electric polarization which could be beneficial for the charge carrier transport.

Overall, in this scenario, we do believe that synergistic efforts in synthesis optimization, discovery of new phases, definition of solid structure-property correlations as a function of chemical composition, as well as definition of novel architectures of chiral HOIP-based devices, would provide the required contribution for the advancement of chiroptoelectronics.

Data availability

No primary research results, software or code have been included and no new data were generated or analysed as part of this review.

Conflicts of interest

There are no conflicts to declare.

Acknowledgements

L. M. acknowledges support from the Ministero dell'Università e della Ricerca (MUR) and the University of Pavia through the program ''Dipartimenti di Eccellenza 2023–2027 and PRIN 2022 Grant No. 2022F2K7J5 with title Two-dimensional chiral hybrid organic–inorganic perovskites for chiroptoelectronics (MIRROR) – CUP B53D23004130006 and Grant No 2022HRZH7P (REVOLUTION) – CUP B53D23015350006 funded by European Union – Next Generation EU. LM and MM acknowledge Fondazione Cariplo through the program ''Young Researchers'', grant no. 2023-1246. This work was supported in part by the Italian Ministry of Foreign Affairs and International Cooperation through project ProPerHP.

Notes and references

1 Z. Y. Wu, B.-L. Jian and H.-C. Hsu, *Opt. Mater. Express*, 2019, **9**, 1882.
2 W.-Y. Liang, F. Liu, Y.-J. Lu, J. Popović, A. Djurišić and H. Ahn, *Opt. Express*, 2020, **28**, 24919.
3 Q. Fu, X. Wang, F. Liu, Y. Dong, Z. Liu, S. Zheng, A. Chaturvedi, J. Zhou, P. Hu, Z. Zhu, F. Bo, Y. Long and Z. Liu, *Small*, 2019, **15**, 1902890.
4 J. Ma, H. Wang and D. Li, *Adv. Mater.*, 2021, **33**, 2008785.
5 X. Wu, M. T. Trinh, D. Niesner, H. Zhu, Z. Norman, J. S. Owen, O. Yaffe, B. J. Kudisch and X.-Y. Zhu, *J. Am. Chem. Soc.*, 2015, **137**, 2089–2096.
6 J. Li, J. Wang, J. Ma, H. Shen, L. Li, X. Duan and D. Li, *Nat. Commun.*, 2019, **10**, 806.
7 M. Yuan, L. N. Quan, R. Comin, G. Walters, R. Sabatini, O. Voznyy, S. Hoogland, Y. Zhao, E. M. Beauregard, P. Kanjanaboos, Z. Lu, D. H. Kim and E. H. Sargent, *Nat. Nanotechnol.*, 2016, **11**, 872–877.
8 S. Ma, J. Ahn and J. Moon, *Adv. Mater.*, 2021, **33**, 2005760.
9 D. G. Billing and A. Lemmerer, *Acta Crystallogr., Sect. E: Struct. Rep. Online*, 2003, **59**, m381–m383.
10 D. G. Billing and A. Lemmerer, *CrystEngComm*, 2006, **8**, 686–695.
11 J. Ahn, E. Lee, J. Tan, W. Yang, B. Kim and J. Moon, *Mater. Horiz.*, 2017, **4**, 851–856.
12 G. Long, R. Sabatini, M. I. Saidaminov, G. Lakhwani, A. Rasmita, X. Liu, E. H. Sargent and W. Gao, *Nat. Rev. Mater.*, 2020, **5**, 423–439.
13 M. Schlipf and F. Giustino, *Phys. Rev. Lett.*, 2021, **127**, 237601.
14 K. Ray, S. P. Ananthavel, D. H. Waldeck and R. Naaman, *Science*, 1999, **283**, 814–816.
15 H. Park, C. Ha and J.-H. Lee, *J. Mater. Chem. A*, 2020, **8**, 24353–24367.
16 C. Coccia, M. Moroni and L. Malavasi, *Molecules*, 2023, **28**, 6166.
17 G. H. Fecher, J. Kübler and C. Felser, *Materials*, 2022, **15**, 5812.
18 H. Lin, C. Zhou, Y. Tian, T. Siegrist and B. Ma, *ACS Energy Lett.*, 2018, **3**, 54–62.
19 L. Zhang, C. Sun, T. He, Y. Jiang, J. Wei, Y. Huang and M. Yuan, *Light: Sci. Appl.*, 2021, **10**, 61.
20 D. G. Billing, *Acta Crystallogr., Sect. E: Struct. Rep. Online*, 2002, **58**, m669–m671.
21 J. Ma, C. Fang, C. Chen, L. Jin, J. Wang, S. Wang, J. Tang and D. Li, *ACS Nano*, 2019, **13**, 3659–3665.
22 J. Wang, C. Fang, J. Ma, S. Wang, L. Jin, W. Li and D. Li, *ACS Nano*, 2019, **13**, 9473–9481.
23 J. Ahn, S. Ma, J.-Y. Kim, J. Kyhm, W. Yang, J. A. Lim, N. A. Kotov and J. Moon, *J. Am. Chem. Soc.*, 2020, **142**, 4206–4212.
24 M.-H. Tremblay, J. Bacsa, B. Zhao, F. Pulvirenti, S. Barlow and S. R. Marder, *Chem. Mater.*, 2019, **31**, 6145–6153.
25 C. Zhou, Y. Chu, L. Ma, Y. Zhong, C. Wang, Y. Liu, H. Zhang, B. Wang, X. Feng, X. Yu, X. Zhang, Y. Sun, X. Li and G. Zhao, *Phys. Chem. Chem. Phys.*, 2020, **22**, 17299–17305.
26 J. Lin, D. Chen, L. Yang, T. Lin, Y. Liu, Y. Chao, P. Chou and C. Chiu, *Angew. Chem., Int. Ed.*, 2021, **60**, 21434–21440.
27 R. Pan, K. Wang and Z.-G. Yu, *Mater. Horiz.*, 2022, **9**, 740–747.
28 S. Ma, Y.-K. Jung, J. Ahn, J. Kyhm, J. Tan, H. Lee, G. Jang, C. U. Lee, A. Walsh and J. Moon, *Nat. Commun.*, 2022, **13**, 3259.
29 R. Lu, Z. Wen, M. Zhao, J. Li, L. Zhang, Y. Yang, H. Jin, Y. Chen, S. Wang and S. Pan, *Adv. Opt. Mater.*, 2023, **11**, 2202290.
30 Y. Zhao, X. Yin, Z. Gu, M. Yuan, J. Ma, T. Li, L. Jiang, Y. Wu and Y. Song, *Adv. Funct. Mater.*, 2023, **33**, 2306199.
31 L. Scalon, J. Brunner, M. G. D. Guaita, R. Szostak, M. Albaladejo-Siguan, T. Kodalle, L. A. Guerrero-León, C. M. Sutter-Fella, C. C. Oliveira, Y. Vaynzof and A. F. Nogueira, *Adv. Opt. Mater.*, 2024, **12**, 2300776.
32 L. Scalon, A. New, Z. Ge, N. Mondal, R. D. Campos, C. Quarti, D. Beljonne, A. F. Nogueira, A. A. Bakulin and Y. Vaynzof, *Chem. Mater.*, 2024, **36**, 4331–4342.
33 H. Kim, C. A. Figueroa Morales, S. Seong, Z. Hu and X. Gong, *ACS Appl. Mater. Interfaces*, 2024, **16**, 16515–16521.
34 C. Yuan, X. Li, S. Semin, Y. Feng, T. Rasing and J. Xu, *Nano Lett.*, 2018, **18**, 5411–5417.
35 K. Trujillo-Hernández, G. Rodríguez-López, A. Espinosa-Roa, J. González-Roque, A. P. Gómora-Figueroa, W. Zhang, P. S. Halasyamani, V. Jancik, M. Gembicky, G. Pirruccio and D. Solis-Ibarra, *J. Mater. Chem. C*, 2020, **8**, 9602–9607.
36 H. Ren, Y. Wu, C. Wang and Y. Yan, *J. Phys. Chem. Lett.*, 2021, **12**, 2676–2681.
37 L. Yan, M. K. Jana, P. C. Sercel, D. B. Mitzi and W. You, *J. Am. Chem. Soc.*, 2021, 18114–18120.
38 Z. Zhang, W. Liang, J. Xue, X. Li, K. Wu and H. Lu, *ACS Nano*, 2024, 12851.
39 J. Son, S. Ma, Y.-K. Jung, J. Tan, G. Jang, H. Lee, C. U. Lee, J. Lee, S. Moon, W. Jeong, A. Walsh and J. Moon, *Nat. Commun.*, 2023, **14**, 3124.
40 M. K. Jana, R. Song, H. Liu, D. R. Khanal, S. M. Janke, R. Zhao, C. Liu, Z. Valy Vardeny, V. Blum and D. B. Mitzi, *Nat. Commun.*, 2020, **11**, 4699.
41 C. Fan, X. Han, B. Liang, C. Shi, L. Miao, C. Chai, C. Liu, Q. Ye and W. Zhang, *Adv. Mater.*, 2022, **34**, 2204119.
42 H. Lu, C. Xiao, R. Song, T. Li, A. E. Maughan, A. Levin, R. Brunecky, J. J. Berry, D. B. Mitzi, V. Blum and M. C. Beard, *J. Am. Chem. Soc.*, 2020, **142**, 13030–13040.
43 C. Coccia, M. Morana, A. Mahata, W. Kaiser, M. Moroni, B. Albini, P. Galinetto, G. Folpini, C. Milanese, A. Porta, E. Mosconi, A. Petrozza, F. De Angelis and L. Malavasi, *Angew. Chem.*, 2024, **136**, e202318557.
44 B. Sun, X.-F. Liu, X.-Y. Li, Y. Zhang, X. Shao, D. Yang and H.-L. Zhang, *Chem. Mater.*, 2020, **32**, 8914–8920.
45 Z. Yu, S. Cao, Y. Zhao, Y. Guo, M. Dong, Y. Fu, J. Zhao, J. Yang, L. Jiang and Y. Wu, *ACS Appl. Mater. Interfaces*, 2022, **14**, 39451–39458.
46 A. Shpatz Dayan, M. Wierzbowska and L. Etgar, *Small Struct.*, 2022, **3**, 2200051.
47 L.-S. Yang, E.-C. Lin, Y.-H. Hua, C.-A. Hsu, H.-Z. Chiu, P.-H. Lo and Y.-C. Chao, *ACS Appl. Mater. Interfaces*, 2022, **14**, 54090–54100.
48 Z. Wen, R. Lu, F. Gu, K. Zheng, L. Zhang, H. Jin, Y. Chen, S. Wang and S. Pan, *Adv. Funct. Mater.*, 2023, **33**, 2212095.
49 Q. Cao, R. Song, C. C. S. Chan, Z. Wang, P. Y. Wong, K. S. Wong, V. Blum and H. Lu, *Adv. Opt. Mater.*, 2023, **11**, 2203125.
50 T. Liu, W. Shi, W. Tang, Z. Liu, B. C. Schroeder, O. Fenwick and M. J. Fuchter, *ACS Nano*, 2022, **16**, 2682–2689.
51 J. Yao, Z. Wang, Y. Huang, J. Xue, D. Zhang, J. Chen, X. Chen, S.-C. Dong and H. Lu, *J. Am. Chem. Soc.*, 2024, **146**, 14157–14165.
52 Y. Zhao, Y. Qiu, J. Feng, J. Zhao, G. Chen, H. Gao, Y. Zhao, L. Jiang and Y. Wu, *J. Am. Chem. Soc.*, 2021, **143**, 8437–8445.
53 M. Yuan, Y. Qiu, Y. Zhao, Y. Zhao, H. Li, X. Wei, G. Chen, J. Feng, H. Gao, J. Zhao, J. Zhao, L. Jiang and Y. Wu, *Sci. China: Chem.*, 2023, **66**, 3602–3610.
54 Y. Peng, X. Liu, L. Li, Y. Yao, H. Ye, X. Shang, X. Chen and J. Luo, *J. Am. Chem. Soc.*, 2021, **143**, 14077–14082.
55 X. Zhang, H. Ye, L. Liang, X. Niu, J. Wu and J. Luo, *ACS Appl. Mater. Interfaces*, 2022, **14**, 36781–36788.
56 Y. Cao, C. Li, J. Deng, T. Tong, Y. Qian, G. Zhan, X. Zhang, K. He, H. Ma, J. Zhang, J. Zhou and L. Wang, *Nano Res.*, 2022, **15**, 7492–7497.
57 B. Yao, Q. Wei, Y. Yang, W. Zhou, X. Jiang, H. Wang, M. Ma, D. Yu, Y. Yang and Z. Ning, *Nano Lett.*, 2023, **23**, 1938–1945.
58 L. Tao, W. Tang, M. Yan, L. Ding, J. Wei, L. Wang, L. Li, L. Li, D. Yang and Y. Fang, *J. Mater. Chem. C*, 2023, **11**, 12392–12399.
59 L. Wang, Y. Xue, M. Cui, Y. Huang, H. Xu, C. Qin, J. Yang, H. Dai and M. Yuan, *Angew. Chem.*, 2020, **132**, 6504–6512.

60 X. Zhang, X. Liu, L. Li, C. Ji, Y. Yao and J. Luo, *ACS Cent. Sci.*, 2021, **7**, 1261–1268.
61 Y. Zhao, Z. Zhou, X. Liu, A. Ren, S. Ji, Y. Guan, Z. Liu, H. Liu, P. Li, F. Hu and Y. S. Zhao, *Adv. Opt. Mater.*, 2023, **11**, 2301239.
62 J. Wu, S. You, P. Yu, Q. Guan, Z.-K. Zhu, Z. Li, C. Qu, H. Zhong, L. Li and J. Luo, *ACS Energy Lett.*, 2023, **8**, 2809–2816.
63 Q. Guan, H. Ye, S. You, Z. Zhu, H. Li, X. Liu and J. Luo, *Small*, 2024, **20**, 2307908.
64 Y. Qin, F.-F. Gao, S. Qian, T.-M. Guo, Y.-J. Gong, Z.-G. Li, G.-D. Su, Y. Gao, W. Li, C. Jiang, P. Lu and X.-H. Bu, *ACS Nano*, 2022, **16**, 3221–3230.
65 Y. Chen, J. Ma, Z. Liu, J. Li, X. Duan and D. Li, *ACS Nano*, 2020, **14**, 15154–15160.
66 Q. Wang, H. Zhu, Y. Tan, J. Hao, T. Ye, H. Tang, Z. Wang, J. Ma, J. Sun, T. Zhang, F. Zheng, W. Zhang, H. W. Choi, W. C. H. Choy, D. Wu, X. W. Sun and K. Wang, *Adv. Mater.*, 2023, 2305604.
67 Y.-H. Kim, Y. Zhai, H. Lu, X. Pan, C. Xiao, E. A. Gaulding, S. P. Harvey, J. J. Berry, Z. V. Vardeny, J. M. Luther and M. C. Beard, *Science*, 2021, **371**, 1129–1133.
68 R. Zhang, Y. Tian, C. Ye, Y. Wang, W. Mi, H. Dai, S. Zou, R. Cao, H. Gao and Y. Xiao, *Chem. Mater.*, 2024, **36**, 3812–3819.
69 C.-H. Yang, S.-B. Xiao, H. Xiao, L.-J. Xu and Z.-N. Chen, *ACS Nano*, 2023, **17**, 7830–7836.
70 G. Jang, D. Jo, S. Ma, J. Lee, J. Son, C. U. Lee, W. Jeong, S. Yang, J. H. Park, H. Yang and J. Moon, *Adv. Mater.*, 2023, 2309335.
71 L. Zhang, S. Hu, M. Guo, Y. Ren, L. Wei, W. Li, F. Lin, Z. Yang, Z. Yang, C. Liu and B. Liu, *Adv. Mater.*, 2023, **35**, 2302059.
72 H. Lee, S. Ma, S. Oh, J. Tan, C. U. Lee, J. Son, Y. S. Park, J. Yun, G. Jang and J. Moon, *Small*, 2023, **19**, 2304166.
73 M. Wang, X. Zhang, L. Liu, X. Zhang, J. Yan, W. Jin, P. Zhang and J. Wang, *ACS Omega*, 2024, 08356.
74 K. Mishra, D. Guyon, J. San Martin and Y. Yan, *J. Am. Chem. Soc.*, 2023, **145**, 17242–17252.
75 Q. Zhuang, H. Li, C. Zhang, C. Gong, H. Yang, J. Chen and Z. Zang, *Adv. Mater.*, 2023, **35**, 2303275.
76 H. Li, C. Zhang, C. Gong, D. Zhang, H. Zhang, Q. Zhuang, X. Yu, S. Gong, X. Chen, J. Yang, X. Li, R. Li, J. Li, J. Zhou, H. Yang, Q. Lin, J. Chu, M. Grätzel, J. Chen and Z. Zang, *Nat. Energy*, 2023, **8**, 946–955.
77 C. Gong, H. Li, H. Wang, C. Zhang, Q. Zhuang, A. Wang, Z. Xu, W. Cai, R. Li, X. Li and Z. Zang, *Nat. Commun.*, 2024 **15**, 4922.